

Partitioning of Ru, Rh, Pd, Re, Ir and Pt between liquid metal and silicate at high pressures and high temperatures - Implications for the origin of highly siderophile element concentrations in the Earth's mantle

Ute Mann^{a,b}, Daniel J. Frost^a, David C. Rubie^{a,*}, Harry Becker^c,
Andreas Audétat^a

^a Bayerisches Geoinstitut, Universität Bayreuth, D-95440 Bayreuth, Germany

^b ETH Zürich, Institut für Geochemie und Petrologie, CH-8092 Zürich, Switzerland

^c Institut für Geologische Wissenschaften, Freie Universität Berlin, D-12249 Berlin, Germany

Received 9 March 2011; accepted in revised form 21 January 2012; available online 7 February 2012

Abstract

The apparent overabundance of the highly siderophile elements (HSEs: Pt-group elements, Re and Au) in the mantles of Earth, Moon and Mars has not been satisfactorily explained. Although late accretion of a chondritic component seems to provide the most plausible explanation, metal–silicate equilibration in a magma ocean cannot be ruled out due to a lack of HSE partitioning data suitable for extrapolations to the relevant high pressure and high temperature conditions. We provide a new data set of partition coefficients simultaneously determined for Ru, Rh, Pd, Re, Ir and Pt over a range of 3.5–18 GPa and 2423–2773 K. In multianvil experiments, molten peridotite was equilibrated in MgO single crystal capsules with liquid Fe-alloy that contained bulk HSE concentrations of 53.2–98.9 wt% ($X_{\text{Fe}} = 0.03\text{--}0.67$) such that oxygen fugacities of $\text{IW} - 1.5$ to $\text{IW} + 1.6$ (i.e. logarithmic units relative to the iron–wüstite buffer) were established at run conditions. To analyse trace concentrations of the HSEs in the silicate melt with LA-ICP-MS, two silicate glass standards (1–119 ppm Ru, Rh, Pd, Re, Ir, Pt) were produced and evaluated for this study. Using an asymmetric regular solution model we have corrected experimental partition coefficients to account for the differences between HSE metal activities in the multicomponent Fe-alloys and infinite dilution. Based on the experimental data, the P and T dependence of the partition coefficients (D) was parameterized.

The partition coefficients of all HSEs studied decrease with increasing pressure and to a greater extent with increasing temperature. Except for Pt, the decrease with pressure is stronger below ~ 6 GPa and much weaker in the range 6–18 GPa. This change might result from pressure induced coordination changes in the silicate liquid. Extrapolating the D values over a large range of potential P – T conditions in a terrestrial magma ocean (peridotite liquidus at $P \leq 60\text{--}80$ GPa) we conclude that the P – T -induced decrease of D would not have been sufficient to explain HSE mantle abundances by metal–silicate equilibration at a common set of P – T -oxygen fugacity conditions. Therefore, the mantle concentrations of most HSEs cannot have been established during core formation. The comparatively less siderophile Pd might have been partly retained in the magma ocean if effective equilibration pressures reached 35–50 GPa. To a much smaller extent this could also apply to Pt and Rh providing that equilibration pressures reached ≥ 60 GPa in the late stage of accretion. With most of the HSE partition coefficients at 60 GPa still differing by 0.5–3 orders of magnitude, metal–silicate equilibration alone cannot have produced the observed near-chondritic HSE abundances of the mantles of the Earth as well as of the Moon or Mars. Our results show that an additional process, such as the accretion of a late veneer composed of some type of chondritic material, was required. The results,

* Corresponding author. Tel.: +49 921 553711; fax: +49 921 553769.

E-mail address: dave.rubie@uni-bayreuth.de (D.C. Rubie).

therefore, support recent hybrid models, which propose that the observed HSE signatures are a combined result of both metal–silicate partitioning as well as an overprint by late accretion.

© 2012 Elsevier Ltd. All rights reserved.

1. INTRODUCTION

The platinum group elements (Ru, Rh, Pd, Os, Ir, Pt), Re and Au are categorised as ‘highly siderophile’ elements (HSEs). This term describes their strong affinity for Fe-metal rather than coexisting silicates at equilibrium, as reflected in extremely high metal–silicate partition coefficients ($\geq 10^4$ – 10^6) at 1 bar. Consequently, during planetary core formation these elements should have been completely removed from a molten silicate mantle by segregating core-forming liquid Fe-alloy. However, in the Earth’s mantle, the concentrations of the HSEs are substantially higher than those predicted from their partitioning behaviour. Moreover, most HSE ratios appear to be near-chondritic, which is inconsistent with their partition coefficients that vary by orders of magnitude at low pressure. This imparts a key role to this group of elements in the understanding of planetary accretion and differentiation: e.g., at which stage of the accretion process were the HSE mantle concentrations established and was core formation already completed by that time?

Theories to explain the HSE abundances in the Earth’s mantle have been developed over the last three decades (see [Richter, 2005](#); [Walker, 2009](#)). The most widely accepted explanation for their apparent ‘overabundance’ is that the HSE concentrations of the mantle were added late in the accretion process, after core formation was complete, in a ‘late veneer’ event. After the proposed giant impact that resulted in the formation of the Moon, core formation terminated on the Earth but accretion still continued with the addition of small amounts of material of chondritic composition. This ‘late veneer’ of oxidised and volatile-rich material would have mixed the HSEs into the mantle and would have established their chondritic proportions. However, improved analytical techniques have revealed that some of the HSE ratios (e.g. Ru/Ir, Pd/Ir) in the primitive upper mantle (PUM) of the Earth are non-chondritic ([Becker et al., 2006](#)). For the mantles of Moon and Mars, similar HSE signatures as for PUM are predicted, though at a much lower concentration level for the Moon (e.g. [Day et al., 2007](#)).

The alternative hypothesis of [Ringwood \(1977\)](#), that the HSE concentrations of the Earth’s mantle could have been established by metal–silicate equilibration if their partition coefficients become substantially lower at high pressures and/or high temperatures, has never been fully discarded (e.g. [Richter et al., 2008](#)). Support came from observations that high-pressure metal–silicate equilibration in a deep magma ocean can explain the abundances of moderately siderophile elements, such as Ni and Co, in the Earth’s mantle (e.g. [Li and Agee, 1996](#); [Richter and Drake, 1997](#); [Gessmann and Rubie, 2000](#); [Wade and Wood, 2005](#); [Kegler et al., 2008](#); [Mann et al., 2009](#); [Rubie et al., 2011](#)). However, the extent to which this might also apply to the HSE con-

centrations of the Earth’s mantle has not yet been fully evaluated. While the solubilities of the HSEs in silicate liquid at 1 bar and moderate temperatures have been intensively studied (e.g. *Ru* - [Borisov and Nachtwey, 1998](#); *Rh* - [Ertel et al., 1999](#); [Fortenfant et al., 2003](#); *Pd* - [Borisov et al., 1994](#); [O’Neill et al., 1995](#); [Laurenz et al., 2010](#); *Re* - [O’Neill et al., 1995](#); [Ertel et al., 2001](#); *Os* - [Fortenfant et al., 2006](#); *Ir* - [Borisov and Palme, 1995](#); [O’Neill et al., 1995](#); *Pt* - [Borisov and Palme, 1997](#); [Ertel et al., 1999](#); [Fortenfant et al., 2003](#); *Au* - [Borisov and Palme, 1996](#)), the number of high-pressure and temperature studies is limited. For some HSEs, the existing studies cover pressures up to 16 GPa at temperatures up to 2423 K (e.g. *Pt*, *Pd* - [Holzheid et al., 2000](#); *Pt* - [Ertel et al., 2006](#); *Pd* - [Richter et al., 2008](#)) and higher-temperature experiments up to 2773 K have been performed at relatively low pressures of ~ 2 GPa (*Pt* - [Cottrell and Walker, 2006](#); *Os* - [Yokoyama et al., 2009](#); *Os*, *Ir*, *Au* - [Brenan and McDonough, 2009](#)). Additionally, the few existing studies performed at higher pressure have focussed on one or two elements only, and the results have led to contradictory conclusions. A distinct decrease of the partition coefficients with increasing pressure and/or temperature was observed for Pd ([Richter et al., 2008](#)), Re ([Richter and Drake, 1997](#)), Pt ([Cottrell and Walker, 2006](#)) and Au ([Danielson et al., 2005](#)) that led [Richter \(2005\)](#) and [Richter et al. \(2008\)](#) to conclude that the mantle concentrations of these HSEs could have resulted from metal–silicate equilibration at the base of a deep magma ocean where pressures of 20–30 GPa prevailed. On the other hand, according to the data of [Holzheid et al. \(2000\)](#) and [Ertel et al. \(2006\)](#) the *P*–*T* induced change of the partition coefficients of Pt and Pd appears to be much weaker. Moreover, while the conclusions of [Richter et al. \(2008\)](#) were derived based on the behaviour of single, less siderophile elements such as Au or Pd alone, the results of [Brenan and McDonough \(2009\)](#) on the partitioning behaviour of Os, Ir and Au clearly show that at least at 2 GPa, Au would still be strongly fractionated from the other two elements, which is in contradiction to the observed near chondritic proportions of the HSEs in the Earth’s mantle. This emphasises the importance of multiple element studies.

Several experimental and analytical difficulties can influence the quality of HSE partitioning data. First, HSE concentrations in silicate melts are generally extremely low, which makes the analysis of mm-size samples from high-pressure experiments difficult. In 1 bar studies, high oxygen fugacities have been used to increase HSE concentrations. Such oxygen fugacities are far above the range applicable for metal–silicate equilibration in a magma ocean (-2 to -4 log units relative to the iron wüstite buffer). Moreover, as valence can vary with f_{O_2} , such studies might derive a much higher valence state for a HSE in the silicate melt than that which applies to magma ocean conditions.

Another experimental obstacle is the occurrence of small metallic nuggets within the silicate liquid, which appear to be a particular problem in experiments performed at more reducing conditions (Ertel et al., 1999, 2006). The origin of nm to μm sized metallic nuggets in the quenched silicates of such experiments has been controversially debated (see Richter, 2005). While Cottrell and Walker (2006) argued for nuggets being a quench phenomenon, Borisov and Palme (1997) and Ertel et al. (1999, 2006) regard nuggets as artefacts resulting from physical or mechanical processes related to the experimental setup or high HSE concentrations in the experimental starting material. If they are artefacts, such nuggets can greatly jeopardize analyses of the quenched silicate glass and result in a drastic overestimation of HSE concentrations. Strong support against the quench origin of nuggets comes from the recent results of Yokoyama et al. (2009) who also observe nuggets in Os partitioning experiments employing natural, very low Os concentrations in both metal and silicate phases. The observed variable Os concentrations could obviously not be explained as a result of quenching from a silicate melt with a uniform Os content. Moreover, comparing results from static piston-cylinder experiments and those obtained with a centrifuging piston-cylinder, Médard et al. (2010) could show that Pt nanonuggets do not form upon quenching but are present in the silicate liquid at run conditions and have a kinetic origin that is favoured by moderate temperatures ($<1900\text{ K}$).

An additional problem might be inherent in the use of various silicate compositions. Most of the previous studies at 1 bar and the high pressure study of Ertel et al. (2006), have determined HSE solubilities, rather than metal–silicate partition coefficients, by equilibrating pure HSE metals with silicate melts. To avoid contamination of the metal, this often involved Fe-free silicate compositions (e.g. anorthite–diopside eutectic composition). On the other hand, Holzheid et al. (2000) had to keep the silicate melting temperature below that of the Fe–Pt and Fe–Pd alloy capsules employed and therefore used an alkali-rich silicate composition ('KNSF' with 18.6 wt% K_2O and 12.4 wt% Na_2O). As element partitioning can be strongly affected by silicate melt structure and composition, results from such studies may not be directly applicable to core formation.

The aim of our study was to determine metal–silicate partition coefficients for a set of HSEs over a wide range of P – T conditions (3.5–18 GPa, 2423–2773 K). By employing multi-HSE bearing alloys, the simultaneous partitioning of Ru, Rh, Pd, Re, Ir and Pt between molten peridotite and liquid Fe-alloy was studied in high pressure multianvil experiments, which in addition allows possible fractionation among the HSEs to be assessed. However, a correction is required to account for the difference in HSE activity-composition relations between the experimental multicomponent Fe-alloys and the infinitely dilute solutions expected in nature. We use a Margules-type formulation and compile thermodynamic parameters to obtain an estimate for the required correction of the experimentally determined partition coefficients for HSE activities. Because of the lack of existing standards for LA-ICP-MS analysis of low HSE concentrations (ppm level) in the quenched

silicates, we have produced silicate glass standards containing 1 to 119 ppm of Ru, Rh, Pd, Re, Ir and Pt. In combination with previous data obtained at lower pressures our new results can be extrapolated to determine if the HSE inventory of the Earth's mantle could have been established by metal–silicate equilibration in a terrestrial magma ocean.

2. EXPERIMENTAL SETUP AND RUN PRODUCTS

The high pressure metal–silicate partitioning behaviour of Ru, Rh, Pd, Re, Ir and Pt was determined experimentally at 3.5–18 GPa and 2423–2773 K using a multianvil apparatus. Metallic Fe–HSE liquids were equilibrated with synthetic peridotite melts contained in MgO single crystal capsules (1.6 mm outer diameter, 2.3 mm length). Details of the run conditions are listed in Table 1. Experiments were performed at 3.5–6 GPa in a 500-tonne Walker-type apparatus and at 18 GPa in a 5000-tonne Kawai-type apparatus (Frost et al., 2004). Tungsten carbide cubes with 11 mm truncation edge lengths were employed with 18 mm edge length Cr_2O_3 -doped octahedral pressure media. The assembly contained a stepped LaCrO_3 heater. The temperature was monitored with type D W_{97}Re_3 – $\text{W}_{75}\text{Re}_{25}$ thermocouples. Based on stable thermocouple readings, the temperature versus power relationship at each pressure was employed to estimate the temperature in cases where thermocouples failed or to extrapolate to temperatures $>2573\text{ K}$ (Table 1). Based on the variation of the temperature–power relationship, temperature uncertainties are $\pm 150\text{ K}$ above and $\pm 100\text{ K}$ below 2573 K. The experiments were quenched rapidly by switching off the electric power to the heater and subsequently decompressed over a few hours. Because the MgO capsules reacted with silicate liquid in the sample, run durations were limited to 70–180 s. Metal–silicate equilibrium should be obtained in this time scale as Mann et al. (2009) found no significant difference between partition coefficients obtained from runs performed for 130 and 300 s at 6 GPa and 2373 K. In addition, results of Thibault and Walter (1995) obtained for Ni and Co partitioning imply that 5 s run times should be sufficient for equilibrium to be obtained at 5 GPa and 2300 K.

Starting materials consisted of 60–66 wt% synthetic peridotite plus 34–40 wt% metal (Table 2). The synthetic peridotite (for preparation see Mann et al., 2009) corresponds to a primitive mantle (PM) composition and contains SiO_2 , MgO , Al_2O_3 , CaO , FeO , TiO_2 , Cr_2O_3 and MnO in the proportions reported by Palme and O'Neill (2003, Table 4). The metal fraction contained Fe plus 47–90 wt.% of the HSEs (equal weight proportions of Ru, Rh, Pd, Re, Ir, Pt) which enabled oxygen fugacity to be varied from -1.5 to $+0.6$ log units relative to the iron–wüstite buffer ($\text{IW} - 1.5$ to $\text{IW} + 0.6$). In preliminary experiments (V347, V348, Z484, Z475) the peridotite powder was mixed together with iron and the individual HSE powders (Table 2, starting compositions D-2 and D-3). In order to reduce the chance of incomplete metal–silicate separation, in subsequent experiments the HSEs were added as pre-alloyed metal chips that were loaded into the centre of the MgO capsules between two layers of powdered peridotite–iron mixtures (Table 2, starting compositions D-2a,

Table 1

Experimental conditions, mol fractions $X_{\text{Fe}}^{\text{metal}}$ and activity coefficients $\gamma_{\text{Fe}}^{\text{metal}}$ of the metals and mol fractions $X_{\text{FeO}}^{\text{silicate}}$ of the quenched silicate melts.

Run	Starting composition	Capsule material	<i>t</i> (s)	<i>P</i> (GPa)	<i>T</i> (K)	log <i>f</i> _{O₂} (ΔIW)	$X_{\text{Fe}}^{\text{metal}}$	$\gamma_{\text{Fe}}^{\text{metal}}$	$X_{\text{FeO}}^{\text{silicate}}$
V364	D-2b	MgO	120	3.5	2773 ^a	−0.97	0.40	0.58	0.07
V363	D-4a	MgO	90	6	2423	−1.48	0.58	0.73	0.06
V347	D-2	MgO	90	6	2423	−0.56	0.38	0.52	0.08
V348	D-3	MgO	90	6	2423	0.56	0.15	0.31	0.07
Z544	D-2a	MgO	180	18	2473 ^a	−0.49	0.37	0.55	0.09
Z538	D-4b	MgO	120	18	2573	−1.46	0.67	0.87	0.08
Z484	D-3	MgO	90	18	2573	0.47	0.14	0.38	0.07
Z541	D-2b	MgO	180	18	2673	−0.89	0.41	0.65	0.08
Z475	D-2	MgO	70	18	2703 ^a	−0.75	0.37	0.63	0.08
Z505	PM	Pt ₇₀ Rh ₃₀ alloy	3600	18	2473 ^a	1.57	0.03	0.19	0.03

t, Run duration; *P*, pressure; *T*, temperature.

*f*_{O₂}: Oxygen fugacity calculated relative to the iron-wüstite (IW) buffer (see Section 4.1.).

MgO = MgO single crystal capsule.

PM: synthetic peridotite (proportions after [Palme and O'Neill, 2003](#)).

^a Derived from temperature vs. power relationship; all other temperatures from thermocouple readings.

Table 2

Compositions of the starting materials (wt%).

HSEs added as:	Mixed powders		Pre-alloyed chips			
	D-2	D-3	D-2a	D-2b	D-4a	D-4b
wt.% HSEs in metal	75	90	76	71	57	47
SiO ₂	27.48	27.48	27.25	29.40	28.37	30.42
MgO	22.26	22.26	22.07	23.81	22.98	24.64
Al ₂ O ₃	2.72	2.72	2.70	2.91	2.81	3.01
CaO	2.21	2.21	2.19	2.36	2.28	2.45
FeO	4.90	4.90	4.86	5.25	5.06	5.43
TiO ₂	0.13	0.13	0.13	0.14	0.13	0.14
Cr ₂ O ₃	0.22	0.22	0.22	0.24	0.23	0.25
MnO	0.08	0.08	0.08	0.09	0.08	0.09
Fe	10.00	4.00	9.69	10.45	16.52	17.71
Ru	5.00	6.00	5.13	4.22	3.59	2.65
Rh	5.00	6.00	5.13	4.22	3.59	2.65
Pd	5.00	6.00	5.13	4.22	3.59	2.65
Re	5.00	6.00	5.13	4.22	3.59	2.65
Ir	5.00	6.00	5.13	4.22	3.59	2.65
Pt	5.00	6.00	5.13	4.22	3.59	2.65

D-2b, D-4a and D-4b). To provide comparable redox conditions, in each experiment the metal chips were weighed and the amount of Fe was adjusted accordingly. The HSE alloy was synthesized in a multianvil press at 4 GPa and 2373 K, starting from HSE metal powders mixed in equal weight proportions.

At run conditions liquid metal separates from silicate melt to form spheres that vary in abundance and size (typically 1–2 large spheres with diameters of 200–460 μm, 0–10 small blobs with diameters of 25–50 μm). The back scattered electron (BSE) image of [Fig. 1a](#) shows a typical run product, here recovered from 3.5 GPa and 2773 K (sample V364), in which a single large metal blob formed. In all samples chemical reaction of the MgO single crystal capsule with the silicate melt resulted in the formation of ferropericlasite at the capsule wall ([Fig. 1a](#)). In some cases ferropericlasite patches also accumulated at the surface of the metal blobs.

In all samples, both metal and silicate developed heterogeneous quench textures. In experiments at ≤6 GPa, the coarse silicate quench textures are dominated by large, elongate, skeletal olivine crystals ([Fig. 1b](#)). The interstitial regions between the olivines consist of a brighter silicate phase in the centre, enriched in Ca and Al and a fine-grained metallic phase that is concentrated along the boundaries of the olivine crystals ([Fig. 1c](#)). We interpret the metallic phase as a quench product with the metal being dissolved in the silicate melt prior to the quench. In samples quenched from 18 GPa, the finer-grained texture of the silicate facilitates quantitative analysis. The quenched metal melts of most samples display dendritic textures and lamellae (e.g. sample Z541, [Fig. 1d](#)). The metal blobs of some samples (V347, V348 and Z484) have very coarse quench textures including zoned grains ([Fig. 1e](#)), which made quantitative analysis difficult.

We also performed one solubility experiment at 18 GPa and 2473 K ([Table 1](#), run Z505), in which peridotite powder was equilibrated in a Pt₇₀Rh₃₀ capsule (1.2 mm outer diameter, 1.4 mm long). As the Pt-solubility study of [Ertel et al. \(2006\)](#) has shown, at this temperature the chosen run time of 60 min should be sufficient to attain equilibrium between solid metal and liquid silicate. The oxygen fugacity of this experiment was IW + 1.6. A section through the run product ([Fig. 1f](#)) shows that the metal capsule did not melt. The silicate melt developed a fine-grained dendritic texture on quenching.

3. ANALYTICAL TECHNIQUES

3.1. Electron microprobe analyses of metals, silicates and ferropericlasite

The metal and the ferropericlasite compositions as well as the major element concentrations of the quenched silicate melts were analysed using a JEOL JXA-8200 electron probe micro-analyzer (EPMA). For all analyses an acceleration voltage of 20 kV and a probe current of 20 nA were employed. The results are listed in [Table 3](#) (metals and

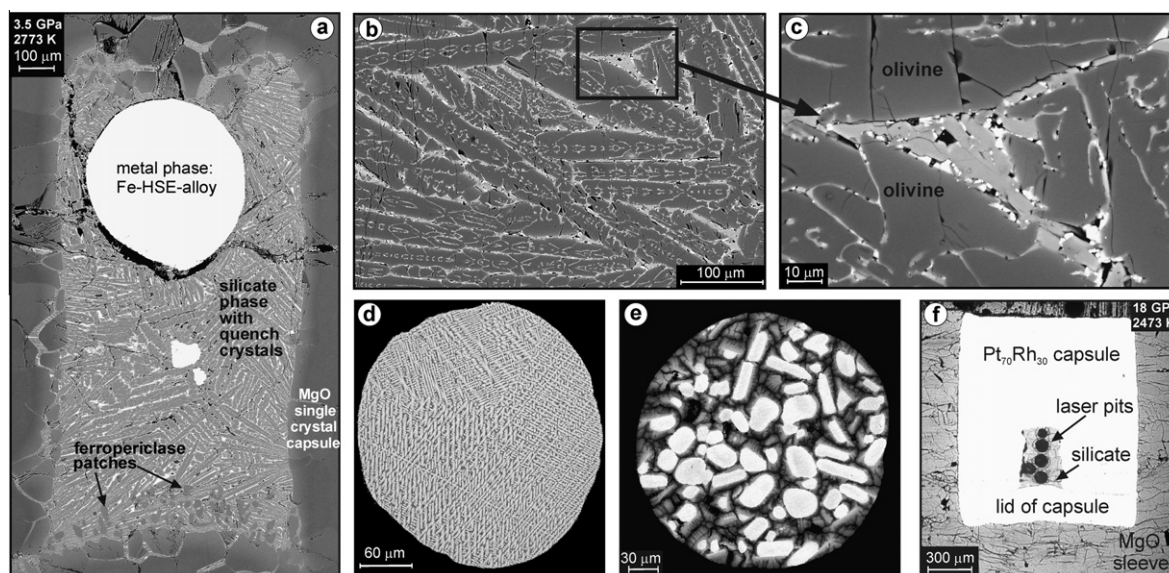


Fig. 1. (a–e) Back scattered electron images showing characteristic features of the run products of liquid metal–liquid silicate partitioning experiments. (a) Section through sample V364 (3.5 GPa, 2773 K) contained in a MgO single crystal capsule. The metal has separated from the silicate liquid at run conditions and formed a sphere. Chemical reaction of the MgO capsule with the silicate liquid leads to formation of ferropericlase patches in the contact zones. (b and c) The silicate quench texture of sample V348 (6 GPa, 2423 K) is representative of all samples run at ≤ 6 GPa. (c) Close up of an interstitial pocket between the large elongated skeletal olivine crystals. The brighter grey matrix is metal that is considered to have been dissolved in the silicate liquid. (d) Dendritic quench patterns like the one in sample Z541 (18 GPa, 2673 K) are typical for most big metal blobs. (e) In some samples the metal blobs have very coarse quench textures like the zoned grains in sample V348 (6 GPa, 2423 K). (f) Reflected light image showing a section through sample Z505 (18 GPa, 2473 K). In this experiment molten peridotite was equilibrated in a Pt–Rh-capsule. The black circles are pits from the LA-ICP-MS analyses (50–70 μm beam diameter).

silicates) and Table 4 (ferropericlase). Errors are given as one standard deviation.

The quenched Fe–HSE alloys were analysed with peak counting times of 20 s for Fe, 40 s for Ru, Rh, Re, Ir, Pt and 60 s for Pd using pure metals as standards. Additionally, we analyzed for Si and Cr, counting for 150 s on the peak position and using andradite and pure Cr as standards. For Ru, Rh and Pd, analysed on a PET crystal, some interference of peaks of the L-series occurs. The flank and positive background of the Rh $L\alpha$ -peak is overlapped slightly by the first order Ru $L\beta$ -peak but a very large overlap of first order Pd $L\alpha$ - and Rh $L\beta$ -peaks excludes both of them for the analysis. Measuring with the Rh $L\alpha$ -peak a value of 2.3 wt% Rh was calculated consistently when analyzing the pure Ru standard. This seems to be rather high, as an overlap of similar degree of the Rh $L\alpha$ -peak in the negative flank part with a second-order Cr $K\alpha$ -peak indicated only 0.2 wt% Rh in the pure Cr standard. We therefore assume that our Ru standard contains a small amount of Rh which was not quantified. However, considering the coarse quench textures of our samples (Fig. 1d and e) the resulting error will be within the analytical uncertainties. Palladium was analysed on the L-peak, which is not ideal as it is interfered by a higher order Rh L-peak resulting in about 0.4 wt% Pd analysed in the pure Rh standard. As this comprises a small error we have ignored it. However, as the intensity of the Pd L-peak is only about half that of the Pd L-peak, we increased the counting times to 60 s.

For each sample, all metal spheres in a section with diameters $\geq 30 \mu\text{m}$ were analysed. Compositions of the small blobs were found to be within the uncertainty range of the average values derived from the large ones. Because of the coarse quench textures of the metals (Fig. 1d and e) all analyses were made with a defocused electron beam (20–30 μm diameter). For metals with a very coarse quench texture (Fig. 2e, samples V347, V348, Z484), analyses were performed along rectangular grids with edge lengths of 100–200 μm so that the analysed areas overlapped. The average of all grid analyses is taken as the bulk composition of the metal. The compositional variation among individual analyses within each grid is generally extremely high, but the standard deviation of such populations certainly does not reflect the real compositional uncertainties. In order to determine a realistic error estimate for the metal compositions of these samples, we divided the analyses in groups of 4–6 and determined the standard deviation among the mean values for the individual groups. The Pt–Rh-capsule of sample Z505 was analysed with a focused electron beam along the rim in proximity to the silicate sample.

The silicates were analysed with peak counting times of 20 s for Si, Mg, Al, Ca and Fe and 100 s for Mn, Cr and Ti and the oxygen content was calculated by stoichiometry. Spinel, MgO, andradite, MnTiO_3 and pure Fe and Cr served as standards. In all cases the electron beam was defocused (30 μm) and coarse textured silicates from experiments at ≤ 6 GPa were analysed on several grids per

Table 3

Average compositions of the quenched silicate and metal melts; table continues on the next page; footnotes for all at bottom of last table.

<i>Silicate</i>	V364 ^a			V363 ^a			V347 ^a			V348 ^a			Z544 ^a							
EPMA (wt%)	No ^b =49	±σ ^c		No = 54	±σ			No = 46	±σ			No = 50	±σ			No = 40	±σ			
Si	16.79	0.17		18.27	0.24			18.02	0.45			18.10	0.42			21.15	0.24			
Mg	30.57	1.08		29.32	0.96			27.10	2.06			27.95	1.66			23.42	0.41			
Al	1.68	0.37		1.64	0.34			2.47	0.78			2.29	0.71			1.95	0.07			
Ca	2.13	0.45		1.98	0.48			3.23	1.03			2.89	0.85			3.05	0.18			
Fe	4.98	0.36		4.41	0.49			5.65	0.99			4.78	0.91			5.39	0.07			
Ti	0.10	0.02		0.10	0.03			0.14	0.04			0.13	0.04			0.14	0.01			
Cr	0.10	0.01		0.11	0.01			0.13	0.02			0.13	0.03			0.15	0.01			
Mn	0.07	0.01		0.07	0.01			0.09	0.02			0.09	0.02			0.10	0.00			
O calc. ^d	43.15	0.27		43.78	0.29			43.65	0.45			43.76	0.35			44.20	0.12			
Total	99.57			99.69				100.47				100.14				99.54				
LA-ICP-MS	No = 4			No = 4				No = 5				No = 5				No = 4				
ppm	HSE-II ^e	±σ ^c	N610 ^e	±σ	HSE-II	±σ	N610	±σ	HSE-I ^e	±σ	N610	±σ	HSE-I	±σ	N610	±σ	HSE-II	±σ	N610	±σ
Ti	–	–	967	17	–	–	935	4	–	–	1358	40	–	–	1271	13	–	–	1315	14
Cr	–	–	936	37	–	–	969	21	–	–	1374	107	–	–	1314	78	–	–	1551	89
Mn	–	–	688	13	–	–	685	11	–	–	1012	63	–	–	950	47	–	–	994	23
Ru	0.3	0.1	–	–	(<0.1) ^f	(0.1)	–	–	0.7	0.5	–	–	1.6	1.2	–	–	0.6	0.1	–	–
Rh	0.9	0.2	0.5	0.1	0.3	0.03	0.2	0.01	3.0	1.9	2.6	2.0	5.0	3.0	3.8	2.2	2.4	0.1	1.9	0.1
Pd	34.6	1.1	36.0	1.9	13.5	1.2	11.0	0.5	16.5	2.5	31.6	3.7	52.2	6.8	88.4	7.4	49.8	4.9	62.7	6.9
Re	1.3	0.1	0.9	0.1	0.2	0.04	0.2	0.047	1.7	0.4	2.7	1.0	8.5	1.8	10.5	2.1	0.8	0.1	0.9	0.1
Ir	0.03 ^f	0.02	–	–	(0.01) ^f	(0.01)	–	–	0.5	0.4	–	–	1.3	1.4	–	–	(0.03) ^f	(0.01)	–	–
Pt	0.9	0.1	0.9	0.1	0.3	0.02	0.2	0.035	1.8	1.3	1.9	1.5	4.1	3.7	3.9	3.3	0.6	0.04	0.6	0.1
<i>Metal</i>	V364			V363				V347 ^a				V348 ^a				Z544				
EPMA (wt.%)	No = 42	±σ ^c		No = 40	±σ			No = 66	±σ			No = 49	±σ			No = 39	±σ			
Fe	22.03	0.65		36.21	0.09			20.99	1.61			7.02	0.77			19.93	0.20			
Ru	13.38	0.87		11.11	0.07			12.54	0.42			15.39	0.54			13.71	0.16			
Rh	14.22	0.15		11.59	0.06			14.96	0.55			17.85	1.11			14.83	0.09			
Pd	13.67	1.52		10.48	0.13			14.22	0.41			13.58	2.67			14.62	0.37			
Re	8.44	0.95		6.83	0.09			13.37	1.60			17.34	0.98			7.99	0.18			
Ir	14.09	0.83		11.49	0.12			12.37	0.40			15.78	2.49			13.72	0.22			
Pt	13.50	0.53		10.93	0.11			12.56	0.15			14.06	0.37			14.35	0.14			
Si	l.o.d. ^g	–		l.o.d.	–			l.o.d.	–			l.o.d.	–			0.07	0.02			
Cr	0.03	0.01		0.05	0.01			0.02	0.01			l.o.d.	0.00			0.03	0.01			
O ^h	–	–		–	–			0.08	0.04			0.42	0.02			–	–			
Total	99.37			98.69				101.11				101.43				99.25				

<i>Silicate</i>	Z538 ^a				Z484 ^a				Z541 ^a				Z475				Z505			
EPMA (wt.%)	No ^b =75		$\pm\sigma^c$		No = 43		$\pm\sigma$		No = 34		$\pm\sigma$		No = 30		$\pm\sigma$		No = 11		$\pm\sigma$	
Si	20.62	0.56			21.08	0.40			20.31	0.40			20.59	0.47			22.18	0.66		
Mg	23.93	0.97			24.79	0.77			24.74	0.62			25.47	0.87			23.90	1.74		
Al	1.96	0.09			1.87	0.05			1.96	0.04			1.76	0.08			2.46	1.52		
Ca	2.68	0.40			2.59	0.29			2.60	0.19			2.37	0.35			3.37	0.67		
Fe	5.23	0.38			4.36	0.13			4.76	0.15			5.08	0.28			1.45	0.26		
Ti	0.12	0.03			0.12	0.01			0.11	0.02			0.11	0.03			0.11	0.03		
Cr	0.13	0.01			0.14	0.01			0.13	0.01			0.13	0.01			0.23	0.07		
Mn	0.08	0.01			0.09	0.01			0.08	0.01			0.08	0.01			0.09	0.02		
O calc. ^d	43.73	0.31			44.45	0.14			43.72	0.24			44.36	0.33			45.16	0.51		
Total	98.49				99.48				98.40				99.95				98.95			
LA-ICP-MS	No = 4				No = 6				No = 4				No = 4				No = 5			
ppm	HSE-II ^e		$\pm\sigma^c$		HSE-I ^e		N610		HSE-II		N610		HSE-I		N610		HSE-I		N610	
Ti	–	–	1254	26	–	–	1259	22	–	–	1122	5	–	–	1067	18	–	–	999	62
Cr	–	–	1419	51	–	–	1353	62	–	–	1353	29	–	–	1278	40	–	–	2187	631
Mn	–	–	872	18	–	–	871	20	–	–	814	10	–	–	764	23	–	–	899	16
Ru	(<0.08)	0.05	–	–	5.4	1.6	–	–	1.1	0.1	–	–	4.7	3.1	–	–	–	–	–	–
Rh	0.5	0.1	0.3	0.04	17.6	3.8	11.0	2.6	4.6	0.2	4.3	0.2	14.5	3.6	9.8	2.6	45.7	6.7	31.0	3.0
Pd	20.9	0.6	25.7	0.6	183	11	247	15	82.3	4.5	113	5	92.1	14.6	140	22	–	–	–	–
Re	<0.1 ^f	0.02	<0.1 ^f	0.01	20.2	4.0	21.5	4.8	1.0	0.1	1.2	0.1	6.2	1.4	7.6	1.6	–	–	–	–
Ir	(<0.01) ^f	0.01	–	–	2.9	3.0	–	–	0.1	0.03	–	–	2.8	4.0	–	–	–	–	–	–
Pt	0.4	0.1	0.5	0.2	6.7	4.3	5.1	3.4	2.4	0.3	2.7	0.4	8.0	6.9	6.0	5.2	7.5	1.3	6.2	0.8
<i>Metal</i>	Z538				Z484 ^a				Z541				Z475				Z505			
EPMA (wt.%)	No = 41		$\pm\sigma^c$		No = 42		$\pm\sigma$		No = 41		$\pm\sigma$		No = 44		$\pm\sigma$		No = 29		$\pm\sigma$	
Fe	46.81	0.26			6.34	0.85			23.11	0.16			20.18	0.25			1.09	0.09		
Ru	9.07	0.09			15.57	0.69			13.19	0.14			13.13	0.11			–	–		
Rh	9.46	0.06			16.96	0.28			14.03	0.09			15.24	0.07			28.10	0.19		
Pd	8.74	0.22			14.23	2.25			13.45	0.28			13.18	0.27			–	–		
Re	5.52	0.12			17.61	1.92			7.98	0.17			13.76	0.33			–	–		
Ir	9.38	0.20			15.88	1.18			13.60	0.21			12.22	0.20			–	–		
Pt	9.05	0.13			14.06	0.62			13.42	0.13			12.22	0.12			69.80	0.26		
Si	0.42	0.04			l.o.d.	–			0.26	0.03			0.21	0.02			l.o.d.	–		
Cr	0.07	0.01			l.o.d.	–			0.04	0.01			0.04	0.01			l.o.d.	–		
O ^h	–	–			–	–			–	–			0.10	0.07			–	–		
Total	98.51				100.66				99.08				100.28				98.98			

^a Analyses were taken along grids as described in the text.

^b No = number of analyses.

^c Errors for EPM analyses are given as one standard deviation of the respective population or of groups of analyses within a grid (see text); Errors for LA-ICP-MS analyses are given as one standard deviation.

^d Oxygen in silicate calculated by stoichiometry.

^e HSE-II, standardisation based on glass HSE-II; HSE-I, standardisation based on glass HSE-I (see electronic annex, Table EA-1); N610, standardisation based on glass NIST 610.

^f Concentration close to the element's detection limit; numbers in brackets are values below the detection limit.

^g l.o.d., limit of detection.

^h Oxygen only analysed in metals of samples V347, V348 and Z475 (40 s peak counting time, MgO standard).

Table 4
Average compositions of ferropericlas.

wt%	V364		V363		V347		V348		Z544		Z538		Z475		Z484		Z541	
	No = 30 $\pm\sigma^a$		No = 24 $\pm\sigma$		No = 16 $\pm\sigma$		No = 13 $\pm\sigma$		No = 27 $\pm\sigma$		No = 30 $\pm\sigma$		No = 9 $\pm\sigma$		No = 15 $\pm\sigma$		No = 32 $\pm\sigma$	
SiO ₂	^b 0.01	0.01	0.05	0.12	0.04	0.02	0.05	0.03	0.11	0.03	0.09	0.04	0.14	0.03	0.11	0.03	0.10	0.03
MgO	92.58	1.05	92.36	1.37	88.76	0.34	90.46	0.78	86.71	0.73	87.18	0.68	88.78	0.67	89.45	0.30	89.11	0.43
Al ₂ O ₃	0.77	0.10	0.92	0.18	1.37	0.04	1.37	0.13	1.34	0.08	1.41	0.10	1.36	0.04	1.45	0.03	1.47	0.08
CaO	0.02	0.01	0.02	0.01	^b 0.02	0.01	0.02	0.01	0.03	0.01	0.03	0.01	0.04	0.01	0.03	0.01	0.03	0.01
FeO	5.86	0.88	6.29	1.06	9.05	0.18	7.53	0.50	11.28	0.60	10.84	0.58	9.23	0.05	8.40	0.08	9.26	0.29
TiO ₂	^b 0.01	0.01	0.03	0.01	^b 0.02	0.01	^b 0.02	0.01	^b 0.02	0.01	0.03	0.01	^b 0.02	0.00	^b 0.02	0.01	^b 0.02	0.01
Cr ₂ O ₃	0.30	0.13	0.22	0.11	0.52	0.02	0.65	0.12	0.39	0.05	0.30	0.03	0.27	0.01	0.36	0.01	0.30	0.02
MnO	0.05	0.01	0.05	0.01	0.07	0.00	0.08	0.01	0.09	0.01	0.08	0.00	0.08	0.00	0.08	0.00	0.07	0.01
Total	99.61		99.93		99.85		100.18		99.97		99.96		99.93		99.90		100.36	

No = number of analyses.

^a Uncertainties are given as one standard deviation of the respective population.

^b Concentration close to the element's detection limit.

sample (150 μ m average length), as described above for the metals, in order to average the compositions of the quench phases.

In all samples that employed MgO single crystal capsules, compositions of the ferropericlas that formed either on the wall of the MgO capsule or as small patches in direct contact with the metal spheres, were determined with peak counting times of 20 s for Mg and Ca, 60 s for Si, Al and Fe and 180 s for Mn, Cr and Ti. Standards were the same as for the silicate analyses. Analyses along the capsule–sample interface were made in areas where a brighter grey tone in the BSE-image due to a higher Fe content indicated a newly-crystallised reaction rim.

3.2. Analysis of the highly siderophile element concentrations in the silicate phase

The HSE concentrations in the quenched silicate melts were determined using laser-ablation inductively coupled plasma mass-spectrometry (LA-ICP-MS) at Bayerisches Geoinstitut. For this purpose, silicate glass standards containing 1 to 119 ppm of Ru, Rh, Pd, Re, Ir and Pt were synthesized. Details of the synthesis, analysis and evaluation of these glasses are given in the electronic annex. The compositions of the two standards, HSE-I and HSE-II, are given in Table EA-1.

The LA-ICP-MS device consists of a Coherent COMP-exPRO 102 excimer laser (ArF, wavelength 193 nm) combined with a Perkin Elmer ELAN DRC-e inductively coupled plasma quadrupole mass-spectrometer device. The sample chamber was flushed with He at a rate of 0.4 l/min and the ICP-MS was tuned to a formation rate of doubly charged ions of $\sim 0.1\%$ and a Th oxide formation rate of $\sim 0.05\%$. Dwell times were 10 ms for major and minor elements and up to 30 ms for the HSEs. For all analyses the laser energy was 80 mJ and signals were collected for 40–50 s, following 30 s of background measurement. The samples were analysed in two sessions for the isotopes ²⁵Mg, ²⁷Al, ²⁹Si, ⁴²Ca, ⁴⁹Ti, ⁵³Cr, ⁵⁵Mn, ⁵⁷Fe, ¹⁰¹Ru, ¹⁰³Rh, ¹⁰⁵Pd, ¹⁸⁵Re, ¹⁹³Ir and ¹⁹⁵Pt. In the first session, HSE-I was used as the standard for samples V347, V348, Z475, Z484 and Z505; in the second session HSE-II was employed for samples V363, V364, Z538, Z541 and Z544.

In both cases a NIST 610 glass standard was additionally included for the measurements and ²⁵Mg served as an internal standard. Samples were analysed in separate blocks, each consisting of 4–5 analyses of the quenched silicate and starting and ending with two analyses of the NIST 610 glass and the respective HSE-doped glass standard. We used laser pit sizes of 50–70 μ m for analysing NIST 610, 50–80 μ m for the HSE standards, and 70–80 μ m for the samples.

The LA-ICP-MS results for the silicates are listed in Table 3 below the major element compositions determined with EPMA. Uncertainties on the values are given as one standard deviation. Additionally, we determined the concentrations of Rh, Pd, Re and Pt in the sample silicates using the NIST 610 glass standard (Sylvester and Eggins, 1997) with ⁴²Ca as the internal standard; the results are listed in Table 3, in the columns labelled N610. For most samples, the latter values agree within $\pm 35\%$ with the results based on the HSE-I and HSE-II standards, but in some cases, mainly for Pd and occasionally for Re and Rh, they deviate by almost 100%. For all subsequent calculations in this study we have exclusively used the values obtained with our glass standards. The N610 columns in Table 3 additionally list Ti, Cr and Mn concentrations in the quenched silicate melts which were also determined using NIST 610 and ⁴²Ca. These concentrations are in good agreement with the EPMA results.

As a quality check for the HSE-analyses employing the new HSE-doped glass standards, we determined the Re, Pd, Pt and Rh concentrations of the NIST 610 glass. The values reported by Sylvester and Eggins (1997) are reproduced within 15% for Re (~ 50 ppm) and within 20–40% for Pt (3.15 ppm), Pd (1.05 ppm) and Rh (1.31 ppm). Employing glass HSE-II in the second session, more accurate results for the NIST 610 glass were achieved than with glass HSE-I. This could be due to the larger pit diameter used in the second session.

Calculated detection limits are 120 ppb for Ru, 40 ppb for Rh, 110 ppb for Pd, 60 ppb for Re, 30 ppb Ir and 80 ppb for Pt. Iridium was below the detection limit in samples V363, Z544, Z538 and Ru in samples V363 and Z538 (Table 3). Moreover, concentrations of Ir in sample V364 and of Re in sample Z538 are quite close to the detection

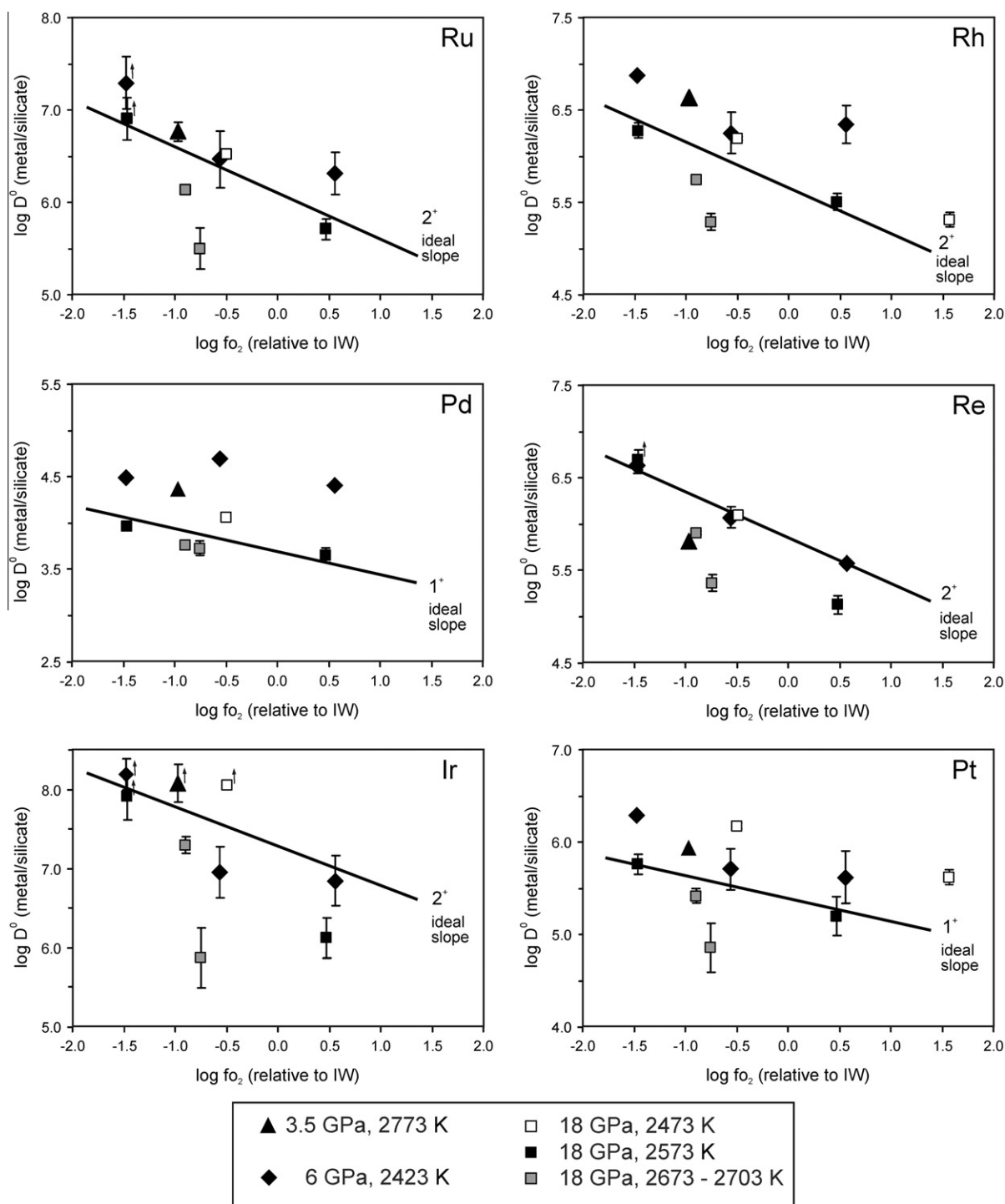


Fig. 2. Logarithmic values of metal-silicate partition coefficients D^0 (mol% basis, corrected to infinite dilution, for details see text) of Ru, Rh, Pd, Re, Ir and Pt plotted as a function of $\log f_{O_2}$ relative to the iron-wüstite buffer (IW). Where no error bars are shown the uncertainties do not exceed the symbol size. The upward-pointing arrows indicate experiments in which the metal concentration in the quenched silicate was close to or below the detection limit and corresponding values are minimum partition coefficients. The lines are plotted with gradients that match the most likely valence (n^+) for each element in the silicate melt, consistent with regressions on the respective isobaric and isothermal data sets using Eq. (12).

limit and the values in Table 3 represent an upper limit. All four samples were equilibrated at relatively low redox conditions (Table 1). However, we used the LOD values in those

samples where the concentrations were below the detection limit. Calculated partition coefficients for the samples mentioned above therefore represent lower-limiting values.

4. RESULTS

4.1. Determination of oxygen fugacity

Equilibration of liquid Fe-bearing alloys with peridotite melt in MgO capsules is accompanied by the formation of ferropericlasite (fp) at the capsule wall, as described above. We therefore utilize the following equilibrium to determine oxygen fugacity:



The experimental oxygen fugacity $\log f_{\text{O}_2}^{\text{exp.}}$ can be derived from the equilibrium constant of Eq. (1) and is expressed relative to the equilibrium between pure Fe metal and “FeO”, i.e. relative to the iron-wüstite (IW) oxygen buffer as:

$$\begin{aligned} \Delta(\text{IW}) &= \log f_{\text{O}_2}^{\text{exp.}} - \log f_{\text{O}_2}^{\text{IW}} \\ &= 2\log \left[\frac{X_{\text{FeO}}^{\text{fp}}}{X_{\text{Fe}}^{\text{metal}}} \right] + 2\log \left[\frac{\gamma_{\text{FeO}}^{\text{fp}}}{\gamma_{\text{Fe}}^{\text{metal}}} \right] \end{aligned} \quad (2)$$

where X and γ are the mole fractions and activity coefficients of the respective components. In Mann et al. (2009) it was also shown that $X_{\text{FeO}}^{\text{fp}}$ can be related to the mole fraction of FeO in the silicate melt $X_{\text{FeO}}^{\text{silicate}}$ through a Fe–Mg exchange coefficient that appears to have a constant value of 0.72 ± 0.05 at ≥ 6 GPa leading to the term:

$$X_{\text{FeO}}^{\text{fp}} = \frac{0.72 X_{\text{FeO}}^{\text{sil}}}{(1 - 0.28 X_{\text{FeO}}^{\text{sil}})} \quad (3)$$

with $X_{\text{FeO}}^{\text{fp}}$ and $X_{\text{FeO}}^{\text{silicate}}$ defined as the molar FeO/(FeO + MgO) ratio of the ferropericlasite and the silicate melt, respectively. This relationship is employed as it also enables the calculation of oxygen fugacities for experiments where FeO-bearing silicate melts were equilibrated in metal or graphite capsules, such as in the solubility experiment Z505 of this study (Pt–Rh-capsule) or the high pressure experiments of Holzheid et al. (2000), Cottrell and Walker (2006) and Righter et al. (2008). High pressure and high temperature data of Frost (2003) were used to express the mixing of FeO in ferropericlasite through:

$$\log(\gamma_{\text{FeO}}^{\text{fp}}) = \frac{(11,000 + 0.011P)(1 - X_{\text{FeO}}^{\text{fp}})^2}{RT \ln(10)} \quad (4)$$

where pressure (P) is in bar, temperature (T) is in K and R is the gas constant. Inserting Eqs. (3) and (4), Eq. (2) can be written as:

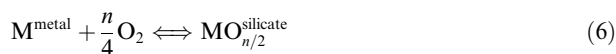
$$\begin{aligned} \Delta(\text{IW}) &= 2\log \left[\frac{0.72 X_{\text{FeO}}^{\text{silicate}}}{X_{\text{Fe}}^{\text{metal}}(1 - 0.28 X_{\text{FeO}}^{\text{silicate}})} \right] \\ &+ \frac{2(11,000 + 0.011P)}{RT \ln(10)} \left(\frac{1 - X_{\text{FeO}}^{\text{silicate}}}{1 - 0.28 X_{\text{FeO}}^{\text{silicate}}} \right)^2 - 2\log(\gamma_{\text{Fe}}^{\text{metal}}) \end{aligned} \quad (5)$$

The broad range of Fe concentrations in the metal alloys requires $\gamma_{\text{Fe}}^{\text{metal}}$ to be evaluated. In the electronic annex, we derive values for $\gamma_{\text{Fe}}^{\text{metal}}$ (Table EA-2) based on a Margules-type asymmetric regular solution model. The results

for ΔIW in each experiment are listed in Table 1 together with the corresponding values of $X_{\text{Fe}}^{\text{metal}}$, $X_{\text{FeO}}^{\text{silicate}}$ and $\gamma_{\text{Fe}}^{\text{metal}}$.

4.2. HSE partition coefficients and valence state

The partitioning of HSEs between metal and silicate is controlled by the redox equilibrium:



where M represents a HSE and n is its valence state in the silicate melt. The equilibrium constant K_6 for Eq. (6) is defined as:

$$\log K_6 = \log \left[\frac{X_{\text{MO}_{n/2}}^{\text{silicate}}}{X_{\text{M}}^{\text{metal}}} \right] + \log \left[\frac{\gamma_{\text{MO}_{n/2}}^{\text{silicate}}}{\gamma_{\text{M}}^{\text{metal}}} \right] - \frac{n}{4} \log f_{\text{O}_2}^{\text{exp.}} \quad (7)$$

based on the respective mole fractions X and activity coefficients γ of the element or oxide in the metal or silicate melt, and the oxygen fugacity of the respective experiment. The $\log f_{\text{O}_2}^{\text{exp.}}$ can be expressed relative to the iron-wüstite buffer (see Eq. (2)) and for any fixed P – T condition, K_6 and $\log f_{\text{O}_2}^{\text{IW}}$ are constants. Moreover, the silicate activity coefficients $\gamma_{\text{MO}_{n/2}}^{\text{silicate}}$ can be regarded as constants assuming that “Henry’s Law” applies to the low HSE concentration range (ppb – ppm range) in the silicate melt and Eq. (7) can then be rearranged to:

$$\log \left[\frac{X_{\text{M}}^{\text{metal}}}{X_{\text{MO}_{n/2}}^{\text{silicate}}} \right] + \log \gamma_{\text{M}}^{\text{metal}} = -\frac{n}{4} \Delta\text{IW} + \text{const.} \quad (8)$$

The molar partition coefficient D for an element M is defined as:

$$D = \left[\frac{X_{\text{M}}^{\text{metal}}}{X_{\text{MO}_{n/2}}^{\text{silicate}}} \right] \quad (9)$$

The partition coefficients determined from experiments performed for this study are reported in Table 5 together with propagated uncertainties. Where HSE concentrations in the silicate are below the detection limit (see Table 3), the D values reported in Table 5 represent lower-limiting values of the partition coefficients only.

Partition coefficients for a metal element between alloys and silicate melts can be considered at three different concentration levels: (1) Where the pure metal is in equilibrium with silicate melt such that $X_{\text{M}}^{\text{metal}} = \gamma_{\text{M}}^{\text{metal}} = 1$ and the solubility $X_{\text{MO}_{n/2}}^{\text{silicate,max}}$ (molar based values) of the metal in the silicate melt is obtained. The equivalent partition coefficient is here referred to as the activity corrected coefficient, $D^{\text{act.cor.}}$, as the metal activity is equal to 1. (2) The partition coefficient obtained for metal alloy concentrations in the wt% range that are outside of the Henry’s law region. This is the case for our experiments where multicomponent alloys with mole fractions of 0.02–0.2 are employed and $\gamma_{\text{M}}^{\text{exp.,metal}}$ values deviate from unity as a function of $X_{\text{M}}^{\text{metal}}$. (3) The partition coefficient at infinite dilution D^0 , where concentrations of the elements of interest are at or below the ppm level and respective $\gamma_{\text{M}}^{\text{metal}}$ values assume the limiting infinite dilution value $\gamma_{\text{M}}^{0,\text{metal}}$. In all three cases a partition coefficient can be formulated according to Eq. (9) and for a fixed

Table 5
Metal-silicate partition coefficients D (mol% based) calculated from experimental results without corrections for metal activities.

Sample	P (GPa)	T (K)	$\log f_{O_2}$ (ΔIW)	Ru	\pm	Rh	\pm	Pd	\pm	Re	\pm	Ir	\pm	Pt	\pm
V364	3.5	2773	-0.97	2.4 * 10 ⁶	6.1 * 10 ⁵	7.6 * 10 ⁵	1.6 * 10 ⁵	9.4 * 10 ³	1.0 * 10 ³	3.1 * 10 ⁵	4.1 * 10 ⁴	2.2 * 10 ⁷	1.7 * 10 ⁷	3.4 * 10 ⁵	4.2 * 10 ⁴
V363	6	2423	-1.48	7.4 * 10 ⁶	6.8 * 10 ⁶	1.6 * 10 ⁶	1.6 * 10 ⁶	1.7 * 10 ⁴	1.4 * 10 ³	1.8 * 10 ⁶	3.9 * 10 ⁵	3.5 * 10 ⁷	2.0 * 10 ⁷	8.6 * 10 ⁵	7.3 * 10 ⁴
V347	6	2423	-0.56	8.4 * 10 ⁵	8.8 * 10 ⁵	2.3 * 10 ⁵	1.5 * 10 ⁵	2.0 * 10 ⁴	3.1 * 10 ³	3.8 * 10 ⁵	1.1 * 10 ⁵	1.3 * 10 ⁶	1.4 * 10 ⁶	1.6 * 10 ⁵	1.1 * 10 ⁵
V348	6	2423	0.56	5.2 * 10 ⁵	3.7 * 10 ⁵	2.0 * 10 ⁵	2.0 * 10 ⁵	6.9 * 10 ³	1.4 * 10 ³	1.1 * 10 ⁵	2.5 * 10 ⁴	6.6 * 10 ⁵	7.1 * 10 ⁵	9.3 * 10 ⁴	8.4 * 10 ⁴
Z544	18	2473	-0.49	1.1 * 10 ⁶	7.8 * 10 ⁴	3.0 * 10 ⁵	1.1 * 10 ⁴	7.0 * 10 ³	7.2 * 10 ²	4.7 * 10 ⁵	3.4 * 10 ⁴	2.3 * 10 ⁷	1.8 * 10 ⁵	6.2 * 10 ⁵	4.7 * 10 ⁴
Z538	18	2573	-1.46	4.4 * 10 ⁶	3.1 * 10 ⁶	7.8 * 10 ⁵	1.3 * 10 ⁵	7.8 * 10 ³	3.0 * 10 ²	2.8 * 10 ⁶	7.9 * 10 ⁵	3.5 * 10 ⁷	3.5 * 10 ⁷	4.0 * 10 ⁵	1.1 * 10 ⁵
Z484	18	2573	-0.75	1.7 * 10 ⁵	4.9 * 10 ⁴	5.4 * 10 ⁴	1.2 * 10 ⁴	2.2 * 10 ³	3.1 * 10 ²	5.0 * 10 ⁴	1.2 * 10 ⁴	2.4 * 10 ⁵	1.9 * 10 ⁵	5.9 * 10 ⁴	3.8 * 10 ⁴
Z541	18	2673	0.47	5.6 * 10 ⁵	2.9 * 10 ⁴	1.4 * 10 ⁵	7.1 * 10 ³	3.8 * 10 ³	2.4 * 10 ²	3.8 * 10 ⁵	1.9 * 10 ⁴	5.4 * 10 ⁶	1.5 * 10 ⁶	1.3 * 10 ⁵	1.9 * 10 ⁴
Z475	18	2703	-0.89	1.3 * 10 ⁵	9.0 * 10 ⁴	5.0 * 10 ⁴	1.2 * 10 ⁴	3.4 * 10 ³	5.4 * 10 ²	1.1 * 10 ⁵	2.4 * 10 ⁴	2.1 * 10 ⁵	2.9 * 10 ⁵	3.7 * 10 ⁴	3.2 * 10 ⁴
Z505	18	2473	1.57			4.5 * 10 ⁴	7.1 * 10 ³							3.4 * 10 ⁵	6.4 * 10 ⁴

f_{O_2} : Oxygen fugacity calculated relative to the iron wüstite (IW) buffer (see section 4.1.).

\pm : Uncertainties determined from error propagation for the calculation of D from the standard deviations of the metal and the silicate concentration.

^a: Minimum value; concentration in silicate close to or below detection limit.

set of P , T and f_{O_2} , the three D values can be related to each other by inserting them in Eq. (8):

$$\begin{aligned} \log [D^{\text{exp.}} \gamma_M^{\text{exp.,metal}}] &= \log [D^0 \gamma_M^{0,\text{metal}}] = \log [D^{\text{act.cor.}}] \\ &= \log \left[\frac{1}{X_{\text{MO}_{n/2}}^{\text{silicate,max}}} \right] \\ &= -\frac{n}{4} \Delta IW + \text{const.} \end{aligned} \quad (10)$$

In this way, for each set of experimental P - T - f_{O_2} , a hypothetical partition coefficient D^0 corresponding to HSE metal concentrations at the level of infinite dilution and thus representative for core-forming alloys can be calculated:

$$D^0 = D^{\text{exp.}} \frac{\gamma_M^{\text{metal}}}{\gamma_M^{0,\text{metal}}} \quad (11)$$

We have estimated values for the required activity coefficients γ_M^{metal} and $\gamma_M^{0,\text{metal}}$ through a Margules-type mixing model (see electronic annex) the results of which are listed in Table EA-2. Employing these parameters we have transformed all our $D^{\text{exp.}}$ values (Table 5), and in the following only refer to D^0 (infinite dilution). The results for D^0 are listed in Table EA-4 of the electronic annex.

Eq. (10) shows that, at a constant P and T , the partition coefficients are related to oxygen fugacity through a relationship that allows the valence state n of the HSEs in the silicate liquid to be obtained by plotting either $\log D^{\text{act.cor.}}$ or, $\log D^0$ versus ΔIW , as demonstrated in Fig. 2 for each HSE. As

$$\log D^0 = -\frac{n}{4} \Delta IW + \text{const}' \quad (12)$$

the respective element's valence n can be derived. We can obtain only an approximation of the valence as only 2–3 isothermal-isobaric data points were obtained. Regressing these data sets the average slope of several sets are -0.55 for Ru, -0.36 for Rh, -0.18 for Pd, -0.66 for Re and -0.29 for Pt which corresponds to valence states of about 2⁺ for Ru, Rh, Re and 1⁺ for Pt and Pd (see Table 6). The solid lines in Fig. 2 show the ideal slopes for these assumed valences. Identical results are obtained employing $D^{\text{act.cor.}}$ instead of D^0 . For most HSEs these values are in good agreement with the valences found in previous solubility studies performed at 1 bar, lower temperatures and over a larger, but higher f_{O_2} range (see compilations of Walter et al. (2000) and Ertel et al. (2008)). However, where solubilities were determined at much higher oxygen fugacities ($\geq IW + 5$), higher valences have been reported for some elements (3⁺ for Ru - Borisov and Nachtweyh, 1998; 2⁺ for Pt - Borisov and Palme, 1997; Ertel et al., 1999; Fortenfant et al., 2003; 4⁺ for Re at up to $IW + 3.0$, Ertel et al., 2001). As several of our Ir partition coefficients are minimum values, the average slope of -0.77 we obtain from data regression, indicating a valence state of 2⁺ to 3⁺, is not very precise. If the D values indicated with arrows in Fig. 2 were even higher the slopes would be steeper and the valence would be closer to 3⁺, which is the valence observed at 1 bar and oxygen fugacities between $IW + 6$ and $+10$ (Borisov and Palme, 1995; Brennan et al., 2005). However, at 2 GPa and oxygen fugacities of $IW - 1.5$ to $+2.7$, i.e. closer

Table 6

Regression coefficients to describe the temperature and pressure dependence of K_D^0 (metal activity corrections applied) according to Eq. (20). Fits were applied separately to data obtained from pressures above and below 6 GPa.

	n^a	P range (GPa)	No. ^b	a	$\pm\sigma^c$	b	$\pm\sigma$	c	$\pm\sigma$
Ru	2^+	0–6	15	1.56	0.05	12760	32	–425	46
		6–18	8	0.64	0.27	12760	32	–63	47
Rh	2^+	0–6	10	–2.22	0.09	22763		–624	60
		6–18	9	–3.75	0.20	22763		–36	33
Pd	1^+	0–6	12	0.86	0.06	10235	126	–426	43
		6–18	8	0.10	0.14	10235	126	–103	25
Re	2^+	0–6	14	0.94	0.19	12760		–438	162
		6–18	7	–0.04	0.15	12760		–26	28
Ir	2^+	0–6	12	1.87	0.20	17526	55	–1077	153
		6–18	5	–0.97	0.64	17526	55	–19	117
Pt	1^+	0–6	53	–3.51	0.06	23824	211	–224	58
		6–18	12	–4.08	0.15	23824	211	–17	29

^a Valence state of the element in the silicate liquid.

^b Number of experimental data points used for the regression.

^c Errors are given as standard deviations from the least square fit. Parameter b was fixed to the value derived from the Gibbs energy data of RuO₂ for Re and to the value derived from the data of Fortenfant et al. (2003) for Rh.

to those of our study, Brenan and McDonough (2009) derived a valence of 1^+ to 2^+ for Ir from solubility experiments. We cannot directly compare our results with those of Brenan and McDonough (2009) because their experiments contained a high proportion of Au in the alloy, which is not considered in our activity model. As their data are in good qualitative agreement with our D^0 values, however, we consider a lower valence state of 2^+ for Ir as more plausible.

As the silicate melt in our experiments does not quench to a glass, nuggets would not be identified visually in the run products. However, as time-resolved LA-ICP-MS spectra of the silicates reveal a uniform distribution of all elements (except for the cases where Ir and Ru concentrations are below the detection limit), we take this as an indicator that the HSEs were homogeneously dissolved in the silicate melt at run conditions. This is supported by the fact that even though the partition coefficients show some scatter in Fig. 2, they do not reach a saturation value towards lower oxygen fugacities (see discussions e.g. in Borisov and Palme (1995) and Ertel et al. (1999)). We take the correlation between $\log D^0$ and ΔIW as a good indicator that the measured HSE concentrations in the quenched silicate liquids result from material that was dissolved in the silicate melts at run conditions and not from the presence of undissolved nuggets.

4.3. The exchange coefficient and effects of pressure and temperature on partitioning

The redox equilibrium controlling the distribution of an element M with valence n between metal and silicate can also be considered relative to the complementary distribution of Fe and FeO through an exchange reaction of the form:



Accordingly, the partition coefficient of element M can be described relative to that of Fe by defining an exchange coefficient K_D , based on the mole fractions X of element and oxide components determined from an experiment:

$$K_D = \frac{[X_M^{\text{metal}}][X_{\text{FeO}}^{\text{silicate}}]^{\frac{n}{2}}}{[X_{\text{MO}_{n/2}}^{\text{silicate}}][X_{\text{Fe}}^{\text{metal}}]^{\frac{n}{2}}} \quad (14)$$

This exchange coefficient is related to the equilibrium constant of reaction (13) through:

$$\log K_{13}(P, T) = \log K_D + \log \left[\frac{[\gamma_M^{\text{metal}}][\gamma_{\text{FeO}}^{\text{silicate}}]^{\frac{n}{2}}}{[\gamma_{\text{MO}_{n/2}}^{\text{silicate}}][\gamma_{\text{Fe}}^{\text{metal}}]^{\frac{n}{2}}} \right] \quad (15)$$

K_D is therefore a function of P , T and the activity coefficients γ of the element and oxide components. The advantage of this analysis is that, provided the valence n of M is correctly determined, K_D is independent of f_{O_2} . As with the partition coefficients, the experimentally determined values, $K_D^{\text{exp.}}$, need to be corrected for Fe and HSE metal activity coefficients (see electronic annex and Table EA-2) in order to obtain the HSE exchange coefficients at the low concentrations relevant for core and mantle compositions. Assuming again that the silicate activity coefficients $\gamma_{\text{MO}_{n/2}}^{\text{silicate}}$ and $\gamma_{\text{FeO}}^{\text{silicate}}$ can be regarded as constants we find the following relationship between $K_D^{\text{exp.}}$ and K_D^0 (the exchange coefficient at infinite dilution):

$$\log K_D^{\text{exp.}}(P, T) + \log \left[\frac{[\gamma_M^{\text{metal}}]}{[\gamma_{\text{Fe}}^{\text{metal}}]^{\frac{n}{2}}} \right] = \log K_D^0(P, T) + \log [\gamma_M^{0, \text{metal}}] \quad (16)$$

For further calculations we only use K_D^0 values that have been obtained from:

$$K_D^0(P, T) = K_D^{\text{exp.}}(P, T) \left[\frac{[\gamma_M^{\text{metal}}]}{[\gamma_M^{0, \text{metal}}][\gamma_{\text{Fe}}^{\text{metal}}]^{\frac{n}{2}}} \right] \quad (17)$$

For comparison with our results, we have also recalculated published HSE partitioning data to obtain K_D^0 values using Eqs. (14) and (17). Additionally, we have converted published solubilities, determined by equilibrating pure HSE metals with Fe-free silicate melts, into equivalent infinite dilution (K_D^0) values. Most of these studies were

performed on Fe-free samples using gas mixing to control oxygen fugacities. The f_{O_2} values can be expressed in terms of $\Delta(IW)$ and can therefore be used to define theoretical Fe and FeO contents in the metal and silicate phase respectively. If we assume ideal mixing of FeO in the silicate melt and a Fe-dominated alloy ($\gamma_{Fe}^{metal} = 1$), Eq. (2) simplifies to:

$$\Delta(IW) = 2 \log \frac{X_{FeO}^{silicate}}{X_{Fe}^{metal}} \quad (18)$$

Starting from solubility data for pure HSE metals (see Section 4.2, $X_{MO_{n/2}}^{silicate,max}$), we have derived values of K_D^0 for the HSEs, corresponding to infinite dilution, based on Eqs. (10), (14), and (18):

$$\begin{aligned} \log K_D^0 &= \log D^0 + \frac{n}{4} \Delta IW \\ &= \log \left[\frac{1}{X_{MO_{n/2}}^{silicate} \gamma_M^{0,metal}} \right] + \frac{n}{4} \Delta IW \end{aligned} \quad (19)$$

As most studies report HSE concentrations in the silicate melt in weight per cent, the mole fractions $X_{MO_{n/2}}^{silicate}$ were estimated by applying a simple weight to mole conversion factor (Borisov et al., 1994). The $\gamma_M^{0,metal}$ values were calculated with the Margules mixing model described in the electronic annex and data for the solid Fe–HSE binaries (Table EA-3). A potential problem in comparing these results with our K_D values is that the solubility experiments have been performed over a wide range and generally at rather high oxygen fugacities ($-0.7 \leq \Delta(IW) \leq +11.3$) which could make the valence state of some HSEs higher than in our study. However, for simplification, we assume that all valence states are as derived in our study (Table 6).

The $\log K_D^0$ values, calculated from experimental data of this study and literature data, are plotted in Fig. 3 as a function of inverse temperature for different pressures. The effects of pressure and temperature on K_D^0 can be described by:

$$\log K_D^0(P, T) = a + \frac{b}{T} + \frac{cP}{T} \quad (20)$$

where a , b and c are constants, T is in K and P in GPa (Righter et al., 1997; Righter and Drake, 2003). Where possible, we fit the temperature dependence from isobaric data sets using data from our study and the literature. In addition, we have determined T -trends of the K_D values using end-member redox exchange reactions for each element at 1 bar. These were derived from thermodynamic data (PdO, Rh₂O₃, RuO₂, IrO₂ - Barin et al., 1989; PtO₂ - Gurvich et al., 1989, ReO₂ - Pownceby and O'Neill, 1994) and were also corrected to infinite dilution using $\gamma_M^{0,metal}$ values calculated with the Margules mixing model (see electronic annex). For comparison, the latter T -trends are plotted as dashed lines in Fig. 3. Except for Rh and Re, their slopes are in good agreement with the T -dependence defined by the experimental data, even though the respective oxides have higher valences in all cases. For Re the experimental data were insufficient to obtain the temperature dependence, but the T -trend derived from the Gibbs energy data of ReO₂ also does not fit with the data. We therefore employed the temperature dependence of the Gibbs energy

related trend of RuO₂ (Fig. 3). For Rh the 1 bar temperature dependence reported by Fortenfant et al. (2003) matches well with our high-pressure data and was used for data regression.

For all HSEs studied, K_D decreases with increasing temperature, with the dependence being strongest for Pt and weakest for Pd. In addition, for most elements, K_D 's at 1 bar are significantly higher than at high pressure, indicating a decrease of K_D with increasing pressure. For Pt this pressure dependence is relatively weak. In order to better resolve the effect of pressure on K_D , we have corrected all data to 2273 K using the derived temperature dependences. The results, as a function of pressure, are plotted in Fig. 4. At pressures where several data were available we employed the mean value of the available K_D 's (at $<IW + 5$). As reported by Borisov and Palme (1995), Ir has an extremely low solubility in the silicate melt and consequently displays the highest K_D values reported here. On the other hand, the K_D values of Pd are at least 1–1.5 orders of magnitude lower than those of the other elements. The K_D values of Pt, Ru and Rh are similar and differ by less than 0.5 log units, which is within the range of uncertainty. The pressure dependences of K_D are similar for all HSEs (except for Pt for which the dependence is relatively weak) and displays a characteristic feature. Upto ~ 6 GPa K_D decreases strongly with increasing pressure whereas in the range 6–18 GPa, the decrease in K_D is much weaker (Fig. 4). This change in pressure dependence is most pronounced for Rh, Ru and Ir and is relatively weak for Re and Pd.

The changes in pressure dependence of K_D at ~ 6 GPa are very similar to results reported for the moderately-siderophile elements Ni and Co by Kegler et al. (2008). In addition, the pressure-dependence of metal–silicate partition coefficients for W may change from positive to negative at 3–4 GPa (Cottrell et al., 2009). The cause of such changes in pressure dependence is not well understood but is likely to be related to pressure-induced coordination changes in the silicate melt structure (e.g. Keppler and Rubie, 1993). The NMR spectroscopy study of Allwardt et al. (2005) for example has shown that in Na-rich aluminosilicate glasses a coordination change of Al occurs between 2–5 GPa. Recent Brillouin and Raman scattering studies on the pressure dependence of MgSiO₃ glass structures indicate that major coordination changes occur at pressures in the range 8–20 GPa (Lee et al., 2008; Sanchez-Valle and Bass, 2010). Such pressure-related coordination changes of the major elements like Si and Al in the silicate melt will change the melt network geometry and could have an influence on the melt's ability to accommodate certain trace cations and thus their affinity for the silicate melt and their partitioning behaviour. As shown in the study of Kegler et al. (2008), pressure-induced changes in partitioning make it unsafe to extrapolate pressure trends determined over small pressure intervals (e.g. 0–2 GPa) to wide ranges of pressure.

To describe the partitioning behaviour of the HSEs as a function of pressure and temperature we have fit the available experimental data (for sources see caption of Fig. 3) using Eq. (20). To account for the two pressure regimes and to avoid an overestimation of the pressure effect

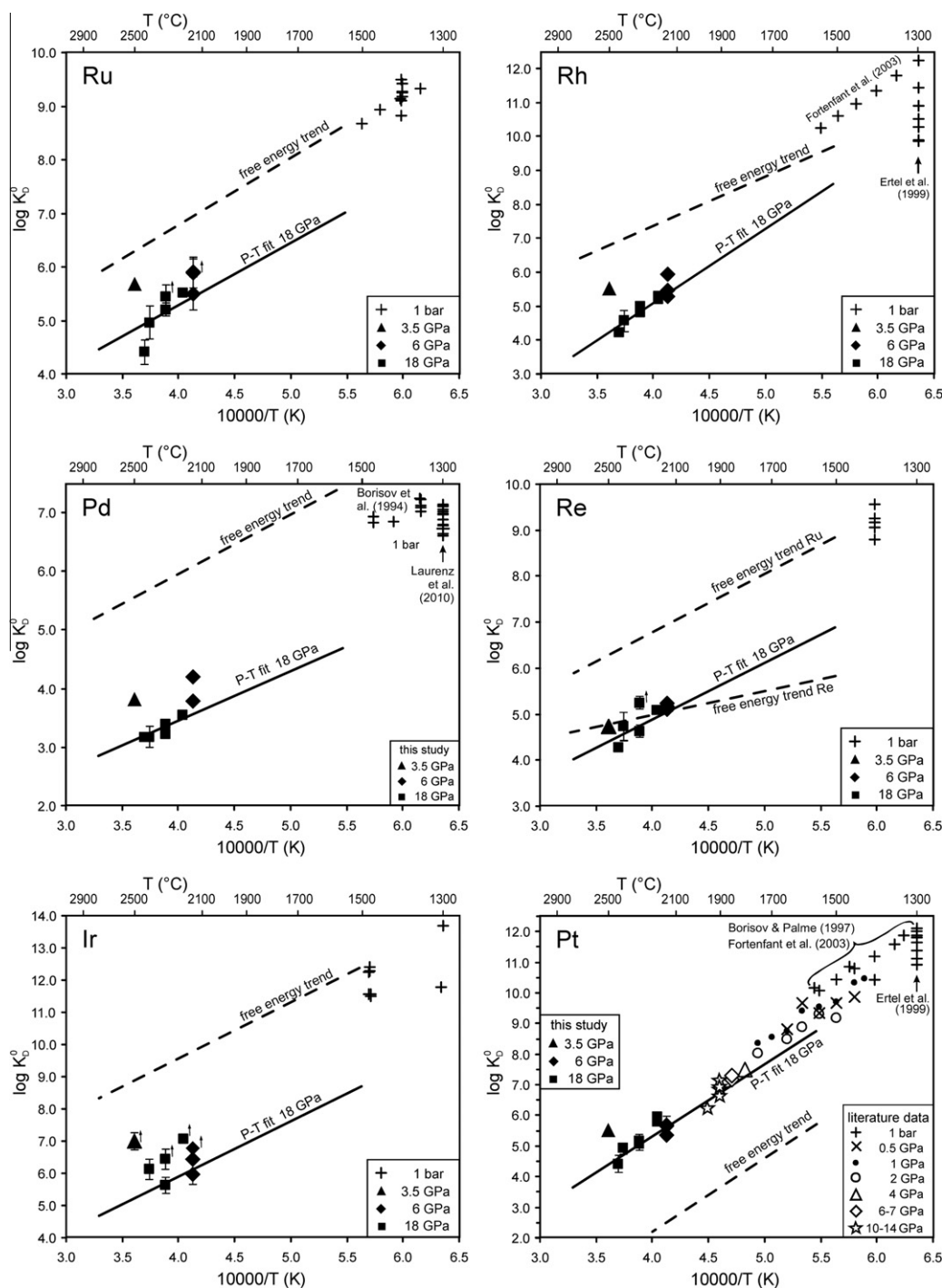


Fig. 3. Logarithmic values of the exchange coefficients K_D^0 (corrected to infinite dilution) of Ru, Rh, Pd, Re, Ir and Pt plotted as a function of inverse temperature ($10,000/T$). Filled black symbols are data from this study. The upward-pointing arrows indicate experiments in which the metal concentration in the quenched silicate was close to or below the detection limit and corresponding values are minimum exchange coefficients. 1 bar data are from: (Ru) Borisov and Nachtwey (1998), data at $+4.9 \leq \Delta(\text{IW}) < +9.3$; (Rh) Ertel et al. (1999), data at $-0.7 < \Delta(\text{IW}) < +4.5$ and Fortenfant et al. (2003), data at $+6.4 < \Delta(\text{IW}) < +8.9$; (Pd) - Borisov et al. (1994), data at $+0.5 \leq \Delta(\text{IW}) \leq +3.2$, Laurenz et al. (2010), data at $+2.4 \leq \Delta(\text{IW}) \leq +4.6$; (Re) - Ertel et al. (2001), data at $+0.4 \leq \Delta(\text{IW}) \leq +1.5$; (Ir) - Borisov and Palme (1995), data at $-0.6 < \Delta(\text{IW}) \leq +4.8$; (Pt) - Borisov and Palme (1997), data at $+2.1 < \Delta(\text{IW}) < +8.0$; Ertel et al. (1999), data at $-0.7 < \Delta(\text{IW}) < +4.5$ and Fortenfant et al. (2003), data at $+6.4 < \Delta(\text{IW}) < +8.9$. Literature data for (Pt) at high pressure are from Ertel et al. (2006), 0.5–14 GPa, $\Delta(\text{IW}) + 1$. The solid lines show the temperature trends at 18 GPa obtained from the data regression (Eq. (20), see text). The dashed lines indicate the Gibbs energy derived trends (corrected for $\gamma_{\text{HSE}}^{\text{metal}}$) for RuO_2 , Rh_2O_3 , PdO , ReO_2 , IrO_2 and PtO_2 , respectively (for references see text). In the Re plot the Gibbs energy related trend of RuO_2 is also shown, which was used to constrain the T -slope while fitting the Re-data (see text).

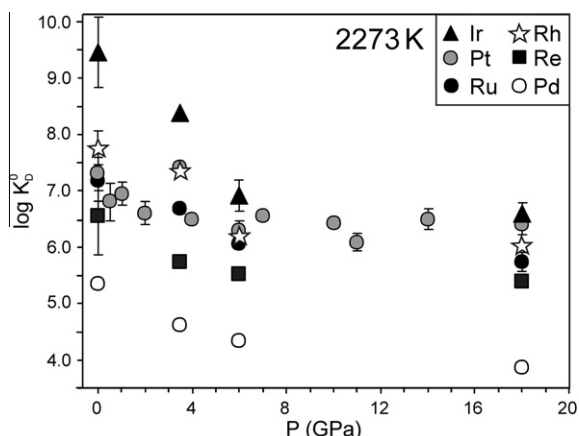


Fig. 4. The logarithmic values of the exchange coefficients K_D^0 (corrected to infinite dilution) of Ru, Rh, Pd, Re, Ir and Pt plotted as a function of pressure at 2273 K using average values for each pressure. 1 bar data include: (Ru) Borisov and Nachtweyh (1998); (Rh) Ertel et al. (1999), Fortenfant et al. (2003); (Pd) Borisov et al. (1994); (Re) Ertel et al. (2001); (Ir) Borisov and Palme (1995); (Pt) Borisov and Palme (1997) and Ertel et al. (1999). High pressure data for Pt are also from Ertel et al. (2006). Where no error bars are shown the uncertainties do not exceed the symbol size.

towards higher pressure, we have performed this fit separately for data from ≤ 6 GPa and >6 GPa in each case assuming the same temperature dependence. The resulting regression coefficients are listed in Table 6. The uncertainties on the regressed parameters are relatively large at ≥ 6 GPa as fewer data are available. As an example, results of the data regression at 18 GPa are shown as solid lines in Fig. 3. As mentioned above, the 1 bar experiments were performed at much higher oxygen fugacities where the

valence of some elements could be higher. As this would result in higher K_D^0 values calculated using Eq. (19), we have limited the 1 bar f_{O_2} range used for regression to results obtained at $<1W + 5$, which limits the possible error on K_D^0 to $\leq +1$ log unit. As a quality test of our regression equations and the activity coefficients calculated with the Margules mixing model, we show in the electronic annex (Section 2, Fig. EA-1) that Pd solubility data from 1 bar experiments determined by Borisov et al. (1994) are well reproduced with our model.

4.4. Compositional effects on partitioning

Some studies in the literature show major deviations both from other data sets and our derived P - T -trends. Such deviations are likely caused by compositional effects, related to either metal or silicate, which are not taken into account in our activity corrections. The K_D values of Pt (2.2 GPa, 2213–2773 K) determined by Cottrell and Walker (2006) and of Pd (1.5 & 12–15 GPa, 1673–2423 K) from Richter et al. (2008) are distinctly lower than our results (Fig. 5). In both cases the experiments were performed mostly in graphite capsules and quenched metals are C-saturated, with C-contents in the range ~ 1 –7 wt%. Previous studies have shown that carbon interacts strongly with some trace elements in Fe-alloys, for example, with W (Cottrell et al., 2009) and with moderately to weakly siderophile elements such as Ti, V and Cr (Mann et al., 2009). C saturated metal concentrations can shift $\log K_D$ and $\log D$ values by an order of magnitude in either direction.

In Fig. 5 two data points of Cottrell and Walker (2006) at 2.2 GPa and 2273 K and 2673 K are consistent with the T -slope derived from our data and from Ertel et al. (2006) but their trend is shifted by about -1 log unit relative to the data of Ertel et al. (2006) obtained at a similar pressure of

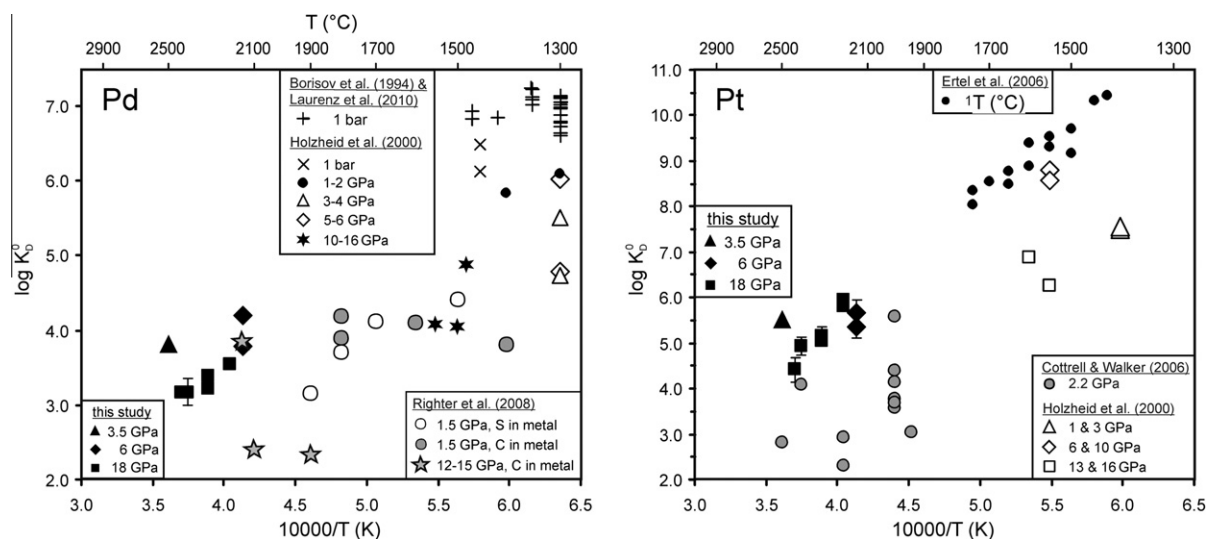


Fig. 5. Compositional effects on the partitioning behaviour of Pd and Pt. Data from this study and for Pd from Borisov et al. (1994), and for Pt from Ertel et al. (2006) were used to derive the P - T trends according to Eq. (20). Comparatively low K_D values for Pd reported by Richter et al. (2008) and for Pt reported by Cottrell and Walker (2006) could result from the presence of C or S in the metal phase, causing the respective HSE to be less siderophile. The lower K_D values for Pd and Pt observed by Holzheid et al. (2000) may result from extremely high alkali contents in the silicate melt (for details see text).

1–2 GPa. This most likely indicates that the presence of 1–5 wt% C in Fe-alloy makes Pt less siderophile. We note, however, that such C concentrations in the metal are high compared to estimates for the C content of the core which are generally less than 1% (e.g. Wood and Halliday, 2010).

Most of the other Pt data of Cottrell and Walker (2006) deviate by -2 to -3 log units from our results and those of Ertel et al. (2006) (Fig. 5). The low K_D values of Cottrell and Walker (2006) and the large scatter in their data (Fig. 5) result from the fact that metallic nuggets were included in the silicate analyses because they were interpreted as quench products. As shown by Médard et al. (2010), nuggets are present at experimental run conditions and must be avoided when analysing the quenched silicate melt (see also Ertel et al., 2006).

Most K_D values for Pd from the study of Richter et al. (2008), performed using both graphite and MgO capsules, are also very low compared with our results (Fig. 5). For experiments run in graphite capsules we presume that interaction with C in the alloy makes Pd less siderophile, as for Pt. Comparing their 1.5 GPa data with our result at 3.5 GPa we can assume a shift by at least 1 log unit in the presence of about 5 wt% C in the alloy. One sample run at 15 GPa matches with our data at higher pressure, but, in addition to C, the alloy contains 28 wt% Sb which may cancel out the effect of C (Fig. 5). On the other hand, the presence of up to 5 wt% S in the metals of C-free samples run in MgO capsules at 1.5 GPa seems to lower K_D to the same extent as observed for C-bearing samples.

Holzheid et al. (2000) studied the partitioning of Pd and Pt between solid Fe-alloy capsules and silicate melts at 1–16 GPa. In order to keep the silicate melting temperature below that of the metal, silicate compositions with high bulk alkali ($K_2O + Na_2O$) contents of 30 wt% were used. Fig. 5 shows that the results for both elements are scattered and are shifted by at least 1 order of magnitude towards lower K_D values compared to our results. Their low values could be the consequence of using alkali-rich melts that have a structure quite different from that of peridotitic melts. Thus alkali-rich silicate melts may make the HSEs much less siderophile and in order to make a comparison with our results corrections for $\gamma_{MOH/2}^{silicate}$ would be required. This effect is weaker for Pd, especially at low pressure (1–2 GPa), but increases with increasing pressure.

Given compositional effects that cannot be corrected for using our mixing model and the fact that some Pt concentrations in the silicates are affected by nuggets, we have not used data from Holzheid et al. (2000), Cottrell and Walker (2006) and Richter et al. (2008) for regression and extrapolations.

5. DISCUSSION

In order to calculate whether high-pressure metal–silicate equilibration in a magma ocean can explain the mantle abundances of HSEs we extrapolate our partitioning results to high pressures and temperatures using the parameterised exchange coefficients K_D (Table 6). The constraints for such calculations are the current HSE concentrations of the upper mantle (Becker et al., 2006) which we assume to

represent the primitive mantle concentrations. In addition, we assume that the Earth has a chondritic bulk composition and that the core encompasses 32 wt% of the Earth's mass (0.17 atomic proportions). Core–mantle partition coefficients $D_{\text{mantle}}^{\text{core}}$ can then be calculated that represent the core to mantle concentration ratio of each element. Based on data of Becker et al. (2006), Fischer-Gödde et al. (2010) and Fischer-Gödde et al. (2011), the range of $D_{\text{mantle}}^{\text{core}}$ values that would be required to explain the mantle HSE concentrations is 400–950 (values based on mol proportions). Assuming that the HSE abundances in the silicate Earth results from metal–silicate partitioning, estimated HSE $D_{\text{mantle}}^{\text{core}}$ values should reflect the cumulative effects of partitioning at all P – T – f_{O_2} equilibration conditions that prevailed during core–mantle differentiation of the Earth. We note that P – T conditions considered in such an approach represent average or “effective” equilibration pressures rather than actual magma ocean depths (Rubie et al., 2003). In addition, recent accretion models imply that core formation was rather a multi-stage process and that the Earth grew by multiple impacts that resulted in one or several magma oceans that increased in depth over time (Wade and Wood, 2005; Rubie et al., 2011).

In order to estimate metal–silicate partition coefficients for HSEs that would result from equilibration in a magma ocean we have used a simple approach and have calculated K_D^0 's at P – T conditions along the peridotite liquidus (Herzberg and Zhang, 1996; Zerr et al., 1998) using the regression coefficients of Table 6. In order to obtain the corresponding partition coefficients D^0 we use Eq. (19) for which an assumption concerning oxygen fugacity is required. Results are shown in Fig. 6a for an oxygen fugacity of IW -2 . This value represents the redox state at the end of core formation and it has been argued that conditions were much more reducing during early stages of accretion (Wade and Wood, 2005; Rubie et al., 2011). Therefore the D^0 values shown in Fig. 6 must be regarded as minimum values.

Fig. 6a shows that the partition coefficients of all HSEs studied decrease as pressure and temperature increase along the peridotite liquidus: i.e. they all become less siderophile as magma ocean depth increases. However, for most HSEs, partition coefficients remain much higher than those required to produce their respective mantle concentrations over a broad range of P – T conditions (≤ 60 GPa, ≤ 3560 K). Thus, metal–silicate equilibration in a magma ocean would result in much greater mantle depletions than those observed. Pd is an exception because, although its partition coefficient shows a P – T dependence that is similar to those of the other elements, the values are 1 to 3 orders of magnitude lower. At an oxygen fugacity of IW -2 , the mantle concentration of Pd could be produced by metal–silicate equilibration at ~ 37 GPa (Fig. 6a); if the oxygen fugacity is reduced to IW -4 , the required pressure is ~ 50 GPa. At a fixed pressure, the partition coefficients of the other HSEs are generally spread over a range of 1.5 orders of magnitude, which is inconsistent with their chondritic ratios in the mantle.

As the partition coefficients shown in Fig. 6a are derived by extrapolating over a large P – T range, we consider the propagated uncertainties (Fig. 6b–e) based on the errors

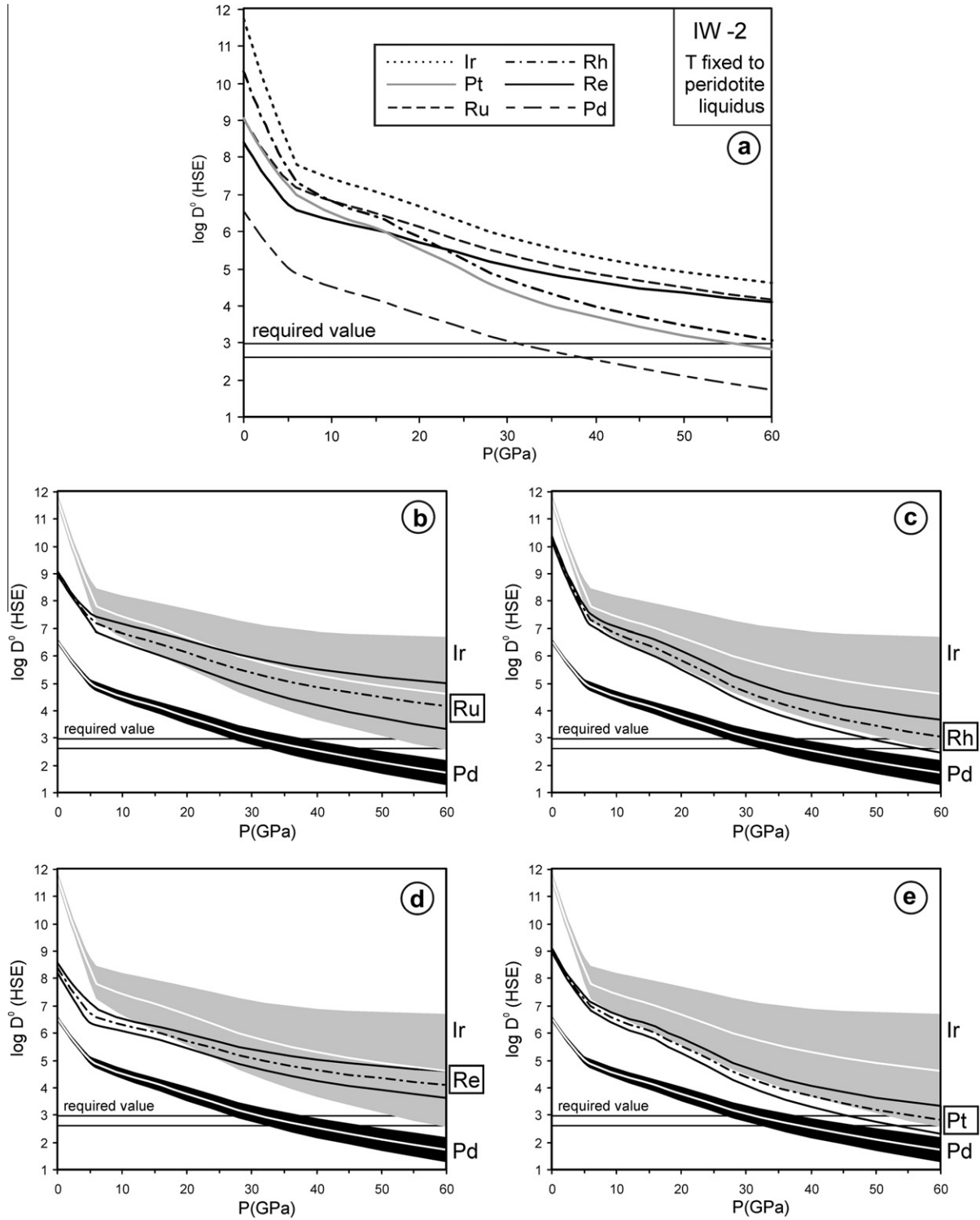


Fig. 6. Logarithmic values of the metal-silicate partition coefficients D^0 of Ru, Rh, Pd, Re, Ir and Pt plotted as a function of pressure. D^0 values are calculated with Eqs. (19) and (20) for P - T conditions at the peridotite liquidus after Herzberg and Zhang (1996) and Zerr et al. (1998) and with the oxygen fugacity fixed to IW -2. (a) Average values of D^0 for each HSE, based on the regression coefficients of Table 6. (b)–(e) are identical plots to (a) but include propagated errors on D^0 based on the uncertainties of the regression coefficients a and c. Stippled lines show the average D^0 values of (b) Ru, (c) Rh, (d) Re, (e) Pt, black solid lines confine the respective error range. Additionally, diagrams (b)–(e) plot the average D^0 values for Ir and Pd with white lines and their error ranges with the grey (Ir) and the black (Pd) shaded areas. The horizontal lines in all diagrams (a)–(e) indicate the allowable range for values of $D^0_{\text{core/mantle}}$ that reproduce the HSE mantle concentrations based on the data of Becker et al. (2006), Fischer-Gödde et al. (2010) and Fischer-Gödde et al. (2011) (for details see text).

on the parameters a , b and c in Eq. (20) as listed in Table 6. In Fig. 6b–e the same relationships are shown as in Fig. 6a, except that log D uncertainty envelopes are included for each element. In each figure, results for Ru, Rh, Re and Pt respectively are plotted together with extrapolated partition coefficients for Ir (the most siderophile element) and Pd (the least siderophile element). Including uncertainties, the pressure range where the Pd mantle concentration could have been produced by metal–silicate equilibration is 30–45 GPa. Total uncertainties are largest for Ir, because its concentration in the silicate melt was below the detection limit in several samples and fewer data were available for regression (Table 6). But even at the lower limit of uncertainty, the Ir mantle concentration could only have been achieved at pressures of ≥ 53 GPa, based on the (unlikely) assumption of oxidising redox conditions throughout accretion. Similarly, the Pt and Rh partition coefficients could only have the required $D_{\text{core/mantle}}$ values at pressures of 50–80 GPa and 50–100 GPa respectively if the oxygen fugacity remained at a constant value of IW -2. The latter value is inconsistent with the observed depletions of moderately siderophile elements (especially V and Cr) which require that core formation initially occurred under highly-reducing conditions, such as IW -4 (Wade and Wood, 2005; Rubie et al., 2011). In the case of Ru and Re, at IW -2 even conditions of 75 and 85 GPa respectively could not have decreased their partition coefficients sufficiently (Figs. 6b, d). At lower oxygen fugacities, the trends for all elements in Fig. 6 would shift to even higher pressures such that at 60 GPa the partition coefficients of Ru, Rh, Re, Ir and Pt still would have been $\geq 10^3$. The resulting mantle concentrations (normalized to CI chondrite) of Re, Ir, Ru, Pt, Rh and Pd based on partition coefficients calculated for conditions of the peridotite liquidus at 5, 20, 40 and 60 GPa and IW -3 respectively, are plotted in Fig. 7. This shows clearly that, except for Pd, the HSEs considered in this study would have been strongly depleted by core formation even at 60 GPa. Thus the observed mantle concentrations could not have been produced by metal–silicate segregation. Additionally, any such conditions would have left a strongly fractionated HSE abundance pattern. This is further supported by the recent results of Brenan and McDonough (2009) on the partitioning behaviour of Ir and two HSEs, Au and Os, not considered in the present work. At 2 GPa, 2173–2588 K, the partition coefficients of Ir and Os differ by 1 order of magnitude and both are about 4–5 orders of magnitude higher than that of Au, which would lead to very different degrees of depletion for these HSEs.

We therefore conclude that the major process that caused the observed near-chondritic HSE abundances of the Earth's mantle cannot be high-pressure, high-temperature metal–silicate equilibration during core formation. The most likely alternative explanation is the late accretion theory, first suggested by Kimura et al. (1974) and Chou (1978), and later established as the 'late veneer' stage in the core formation model of O'Neill (1991). According to this hypothesis, the HSEs were almost entirely removed from a planetary mantle as long as metal–silicate segregation was occurring, but were replenished by the late

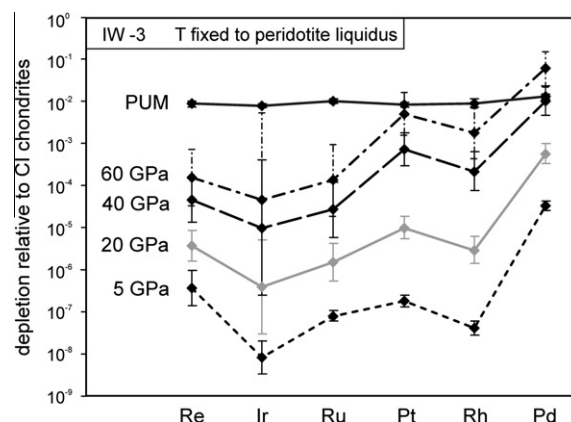


Fig. 7. Highly siderophile element concentrations, normalised to CI chondrite (Fischer-Gödde et al., 2010), predicted for the primitive upper mantle (PUM, data from Becker et al., 2006; Rh from Fischer-Gödde et al., 2011) as a result of metal–silicate partitioning at various P – T conditions in a magma ocean. Partition coefficients were calculated at the pressures indicated and at the respective peridotite liquidus temperatures (Herzberg and Zhang, 1996; Zerr et al., 1998) and at an oxygen fugacity of IW -3, using Eqs. (19) and (20) together with the regression coefficients from Table 6. From these partition coefficients the magma ocean concentrations were calculated employing a mass balance equation and assuming a chondritic bulk composition for the Proto-Earth and a constant molar proportion of 16.6% for the core (all data employed are based on molar proportions).

accretion of small amounts (e.g. for the Earth 0.09–0.5% of its mass) of some type of primitive meteoritic material after core formation had ceased. The late veneer is additionally discussed as a potential source of planetary water, carbon and other highly volatile elements. Although many details of the late veneer are poorly understood, it provides a plausible explanation for the enigmatic presence and relative proportions of the HSEs in the silicate portions of the Earth, Moon and Mars (see Walker (2009) for a recent review).

Models have also been proposed that combine late accretion and high-pressure equilibration. Based on partitioning data for Pd, Au (Danielson et al., 2005) and Pt (Cottrell and Walker, 2006), Richter et al. (2008) proposed that mantle concentrations of these HSEs could have been established at high pressure and temperatures in a magma ocean, while the extremely siderophile elements Ir, Os, Ru and Rh would have been depleted from the mantle during this equilibration period. Afterwards, a late veneer would have delivered material with about chondritic proportions of HSEs that overprinted the previously set signature by introducing Ir, Os, Ru and Rh and slightly increasing the concentrations of Pd and possibly Au. This would provide an explanation for the somewhat suprachondritic concentrations of Pd and the enstatite chondrite like Au/Ir (e.g. Fischer-Gödde et al., 2011). Our data support a partial retention of Pd during high pressure equilibration and its subsequent supplement by material of the late veneer such that the suprachondritic Pd/Ir mantle ratio could be explained. However, at all P – T conditions our data designate Ru as the second most siderophile element among the

investigated HSEs and it is unlikely that the observed suprachondritic Ru/Ir or Ru/Pt ratios (Becker et al., 2006) result from partial retention of Ru during equilibration but rather reflect the nature of the accreted material. The 2 GPa partitioning data of Brenan and McDonough (2009) for Ir, Os and Au would support a hybrid model resulting in suprachondritic Au/Ir or Au/Os ratios, but this is not what is observed in peridotites. Unlike the data of Cottrell and Walker (2006) and Righter and Drake (1997), our results do not indicate that the P – T induced decrease of the Pt and Re partition coefficients would have been strong enough to substantially retain them in the mantle during metal–silicate segregation although for Pt a trace amount might have remained in a magma ocean at pressures >60 GPa. Re, on the other hand, must belong to the group of HSEs (Ir, Os, Ru, Rh) that was added to the mantle only with the late veneer. This is important as the Re/Os ratio is mirrored by the $^{187}\text{Os}/^{188}\text{Os}$ ratio, which is elevated in the Earth's mantle compared to carbonaceous chondrites. With Re being very siderophile this cannot result from partial retention of Re in the magma ocean but must rather be linked to an elevated Re/Os ratio in the material added in the late accretion period. This would exclude certain material of the meteoritic record, especially carbonaceous chondrites as a potential source material for the late veneer, which on the other hand would be possible candidates for the supply of highly volatile components such as water. Therefore, refining such hybrid models, which in accordance with our new HSE partitioning data seem to provide the most likely explanation for the HSE inventory of the mantles of the Earth and other planetary bodies, requires much better constraints on the origin and composition of the late accreted material.

6. SUMMARY AND CONCLUSIONS

The aim of this study was to test whether high temperatures and/or high pressures drastically change the partitioning behaviour of the highly siderophile elements observed at 1 bar. We have therefore experimentally determined the partitioning behaviour of Ru, Rh, Pd, Re, Ir and Pt between liquid Fe-rich metal and peridotitic melt over a range of 3.5–18 GPa, 2423–2773 K and oxygen fugacities of -1.5 to $+1.6$ log units relative to the iron-wüstite buffer. Experiments were performed using MgO single crystal capsules thus avoiding contamination of the alloy with C (for example), which can lead to undesirable compositional effects.

For the analysis of trace concentrations of the HSEs in the silicate liquid in-house glass standards were produced and carefully calibrated and evaluated. The analyses of the sample silicates were performed using LA-ICP-MS techniques. The best results were achieved employing large ablation pits of 80 μm diameter and relatively high ablation rates of 15–20 Hz. Using this technique the detection limit of the HSEs ranges from 30–120 ppb and was reached in some samples for the elements Ir and Ru, which have the lowest solubilities in silicate melts.

We have corrected experimentally determined HSE partition coefficients to infinite dilution such that they can be employed for regression and extrapolation at the low

concentration levels relevant during core formation. For this we employed a multicomponent Margules type asymmetric regular solution model and have compiled a list of Margules interaction parameters for binary Fe–HSE and HSE–HSE systems that can be used to calculate metal activity coefficients as a function of pressure and temperature.

A linear increase of the logarithmic values of the partition coefficients of all HSEs with decreasing oxygen fugacity indicates the presence of HSE ions in the silicate melt. This allows their valence state to be determined and indicates strongly that our results are not contaminated by the presence of metallic nuggets in the silicate melt.

All HSEs studied were found to become less siderophile with both increasing temperature and increasing pressure, with the effect of temperature being much stronger. At pressures above 5–6 GPa, we observe a change from a strong to a much weaker decrease of the HSE exchange coefficients (K_D) that resembles the partitioning behaviour of the siderophile elements Ni and Co (Kegler et al., 2008). We assume this change to be related to a change in the coordination of major elements in the silicate melt over the pressure range.

Given the distinctly weaker effect of pressure on partitioning at pressures >6 GPa we have fit P – T dependent expressions of K_D separately to the data from the two pressure regimes. The derived regression coefficients were employed to extrapolate HSE partition coefficients to pressures and temperatures representative of conditions in a deep magma ocean.

Our results show that even very high P – T conditions (e.g. 60 GPa, 3560 K) could not efficiently decrease the partition coefficients of Ru, Re and Ir to a level such that their observed mantle concentrations could be explained by equilibration in a deep magma ocean. In contrast, for Pd, the least siderophile among the studied HSEs, we observe that at high effective equilibration pressures of 35–50 GPa the required D value could have been matched. Considering the range of uncertainty for our extrapolations, this might as well be the case for Pt and Rh, although at higher pressures of at least 53–63 GPa. At any of these pressures, the partition coefficients of all HSEs differ by at least 1–2 orders of magnitude and the partition coefficient of Pd is consistently lower by 1–3 orders of magnitude compared to all other HSEs. Therefore, our results show that high P – I equilibrium partitioning during core formation would have depleted the HSEs from a magma ocean to different extents and resulted in almost complete removal of most of them.

However, there still remain some unresolved questions concerning a 'late veneer' scenario which generally provides a good explanation for the establishment of near-chondritic HSE ratios in the mantle of the Earth but also the Moon, Mars and maybe even Vesta. The fact that some of the relative HSE proportions are slightly suprachondritic might be used to constrain the composition of the material added with the late veneer, e.g. if within the sample set, meteorites were found that had the same elevated ratios compared to carbonaceous chondrites. On the other hand, suprachondritic HSE ratios might be reconciled by current models that explain the HSE mantle abundances and proportions by adding up the signatures of both equilibrium

partitioning and late accretion. The first process could have retained some Pd, Au and maybe trace amounts of Pt which after adding a chondritic late veneer HSE inventory to the mantle is recorded as a slightly suprachondritic Pd/Ir ratio. However, based on our new partitioning data, such a hybrid model cannot explain suprachondritic Ru/Ir. To quantify the contribution of each of the end member processes will require better constraints on the origin and thus composition of the late veneer as well as a better resolution of the timing of late accretion and of differentiation of individual planetary bodies.

ACKNOWLEDGMENTS

Etienne Médard is thanked for discussions about the nugget effect and about his latest data on Pt partitioning. We are grateful for helpful comments from James Brenan and acknowledge the review of Dave Walker. This work was supported by the “Elitenetzwerk Bayern” graduate programme “Structure, Reactivity and Properties of Oxide Materials” at Bayerisches Geoinstitut and by the German Research Foundation (Be 1820/3-1).

APPENDIX A. SUPPLEMENTARY DATA

Supplementary data (“Electronic Annex”) associated with this article can be found, in the online version, at doi:10.1016/j.gca.2012.01.026.

REFERENCES

- Allwardt J. R., Stebbins J. F., Schmidt B. C., Frost D. J., Withers A. C. and Hirschmann M. M. (2005) Aluminum coordination and the densification of high-pressure aluminosilicate glasses. *Am. Mineral.* **90**, 1218–1222.
- Barin I., Sauert F., Schultze-Rhonhof E. and Sheng W. S. (1989) *Thermochemical Data of Pure Substances, Part I and Part II*. Verlagsgesellschaft Weinheim, Germany, 1739pp.
- Becker H., Horan M. F., Walker R. J., Gao S., Lorand J.-P. and Rudnick R. L. (2006) Highly siderophile element composition of the Earth’s primitive upper mantle: constraints from new data on peridotite massifs and xenoliths. *Geochim. Cosmochim. Acta* **70**, 4528–4550.
- Borisov A. and Nachtwey K. (1998) Ru solubility in silicate melts: experimental results in oxidizing region. *LPSC XXIX conf. abstr.*, 1320.
- Borisov A. and Palme H. (1995) The solubility of iridium in silicate melts: new data from experiments with Ir₁₀Pt₉₀ alloys. *Geochim. Cosmochim. Acta* **59**, 481–485.
- Borisov A. and Palme H. (1996) Experimental determination of the solubility of Au in silicate melts. *Mineral. Petrol.* **56**, 297–312.
- Borisov A. and Palme H. (1997) Experimental determination of the solubility of platinum in silicate melts. *Geochim. Cosmochim. Acta* **61**, 4349–4357.
- Borisov A., Palme H. and Spettel B. (1994) Solubility of palladium in silicate melts – Implications for core formation in the Earth. *Geochim. Cosmochim. Acta* **58**, 705–716.
- Brenan J., McDonough W. F. and Ash R. (2005) An experimental study of the solubility and partitioning of iridium, osmium and gold between olivine and silicate melt. *Earth Planet. Sci. Lett.* **237**, 855–872.
- Brenan J. M. and McDonough W. F. (2009) Core formation and metal-silicate fractionation of osmium and iridium from gold. *Nat. Geosci.* **2**, 798–801.
- Chou C. L. (1978) Fractionation of siderophile elements in the Earth’s upper mantle. *Proc. 9th. Lunar Planet. Sci. Conf.*, 219–230.
- Cottrell E. and Walker D. (2006) Constraints on core formation from Pt partitioning in mafic silicate liquids at high temperatures. *Geochim. Cosmochim. Acta* **70**, 1565–1580.
- Cottrell E., Walter M. J. and Walker D. (2009) Metal-silicate partitioning of tungsten at high pressure and temperature: implications for equilibrium core formation in Earth. *Earth Planet. Sci. Lett.* **281**, 275–287.
- Danielson L. R., Sharp T. G. and Hervig R. L. (2005) High P and T partitioning of Au: constraints on core formation. *36th Lunar Planet. sci. conf.* 1955 (abstr.).
- Day J. M. D., Pearson D. G. and Taylor L. A. (2007) Highly siderophile element constraints on accretion and differentiation of the Earth–Moon system. *Science* **315**, 217–219.
- Ertel W., Dingwell D. B. and Sylvester P. J. (2008) Siderophile elements in silicate melts – A review of the mechanically assisted equilibration technique and the nanonugget issue. *Chem. Geol.* **248**, 119–139.
- Ertel W., Drake M. J., Walter M. J. and Sylvester P. J. (2006) Experimental study of platinum solubility in silicate melt to 14 GPa and 2273 K: implications for accretion and core formation in Earth. *Geochim. Cosmochim. Acta* **70**, 2591–2602.
- Ertel W., O’Neill H. S. C., Sylvester P. J. and Dingwell D. B. (1999) Solubilities of Pt and Rh in a haplobasaltic silicate melt at 1300 °C. *Geochim. Cosmochim. Acta* **63**, 2439–2449.
- Ertel W., O’Neill H. S. C., Sylvester P. J., Dingwell D. B. and Spettel B. (2001) The solubility of rhenium in silicate melts: implications for the geochemical properties of rhenium at high temperatures. *Geochim. Cosmochim. Acta* **65**, 2161–2170.
- Fischer-Gödde M., Becker H. and Wombacher F. (2010) Rhodium, gold and other highly siderophile element abundances in chondritic meteorites. *Geochim. Cosmochim. Acta* **74**, 356–379.
- Fischer-Gödde M., Becker H. and Wombacher F. (2011) Rhodium, gold and other highly siderophile elements in orogenic peridotites and peridotite xenoliths. *Chem. Geol.* **280**, 365–383.
- Fortenfant S. S., Günther D., Dingwell D. B. and Rubie D. C. (2003) Temperature dependence of Pt and Rh solubilities in a haplobasaltic melt. *Geochim. Cosmochim. Acta* **67**, 123–131.
- Fortenfant S. S., Dingwell D. B., Ertel-Ingrisch W., Capmas F., Birk J. L. and Dalpé C. (2006) Oxygen fugacity dependence of Os solubility in haplobasaltic melt. *Geochim. Cosmochim. Acta* **70**, 742–756.
- Frost D. J. (2003) Fe²⁺–Mg partitioning between garnet, magnetite, and (Mg, Fe)₂SiO₄ phases of the transition zone. *Am. Mineral.* **88**, 387–397.
- Frost D. J., Poe B. T., Trønnes R. G., Liebske C., Duba A. and Rubie D. C. (2004) A new large-volume multianvil system. *Phys. Earth Planet. Inter.* **143–144**, 507–514.
- Gessmann C. K. and Rubie D. C. (2000) The origin of the depletions of V, Cr and Mn in the mantles of the Earth and Moon. *Earth Planet. Sci. Lett.* **184**, 95–107.
- Gurvich L. V., Veyts I. V. and Alcock C. B. (1989). , Fourth edition.
- Herzberg C. and Zhang J. Z. (1996) Melting experiments on anhydrous peridotite KLB-1: compositions of magmas in the upper mantle and transition zone. *J. Geophys. Res. – Solid Earth* **101**, 8271–8295.
- Holzheid A., Sylvester P., O’Neill H. S. C., Rubie D. C. and Palme H. (2000) Evidence for a late chondritic veneer in the Earth’s mantle from high-pressure partitioning of palladium and platinum. *Nature* **406**, 396–399.
- Kegler P., Holzheid A., Frost D. J., Rubie D. C., Dohmen R. and Palme H. (2008) New Ni and Co metal-silicate partitioning data

- and their relevance for an early terrestrial magma ocean. *Earth Planet. Sci. Lett.* **268**, 28–40.
- Keppeler H. and Rubie D. C. (1993) Pressure-induced coordination changes of transition-metal ions in silicate melts. *Nature* **364**, 54–56.
- Kimura K., Lewis R. S. and Anders E. (1974) Distribution of gold and rhenium between nickel-iron and silicate melts – Implications for abundance of siderophile elements on Earth and Moon. *Geochim. Cosmochim. Acta* **38**, 683–701.
- Laurenz V., Fonseca R. O. C., Ballhaus C. and Sylvester P. J. (2010) Solubility of palladium in picritic melts: 1. The effect of iron. *Geochim. Cosmochim. Acta* **74**, 2989–2998.
- Lee S. K., Lin J.-F., Cai Y. Q., Hiraoka N., Eng P. J., Okuchi T., Mao H.-k., Meng Y., Hu M. Y., Chow P., Shu J., Li B., Fukui H., Lee B. H., Kim H. N. and Yoo C.-S. (2008) X-ray Raman scattering study of MgSiO_3 glass at high pressure: implication for triclustered MgSiO_3 melt in Earth's mantle. *Proc. Natl. Acad. Sci.* **105**, 7925–7929.
- Li J. and Agee C. B. (1996) Geochemistry of mantle-core differentiation at high pressure. *Nature* **381**, 686–689.
- Médard E., Schmidt M. W., Wälle M., Keller N. S. and Günther D. (2010) HSE partitioning and core formation: solving the nanonugget issue. *EMPG XIII*, Toulouse, April 11–14.
- Mann U., Frost D. J. and Rubie D. C. (2009) Evidence for high-pressure core-mantle differentiation from the metal-silicate partitioning of lithophile and weakly-siderophile elements. *Geochim. Cosmochim. Acta* **73**, 7360–7386.
- O'Neill H. S. C. (1991) The origin of the moon and the early history of the earth - a chemical model. Part 2: the Earth. *Geochim. Cosmochim. Acta* **55**, 1159–1172.
- O'Neill H. S. C., Dingwell D. B., Borisov A., Spettel B. and Palme H. (1995) Experimental petrochemistry of some highly siderophile elements at high temperatures, and some implications for core formation and the mantle's early history. *Chem. Geol.* **120**, 255–273.
- Palme H. and O'Neill H. S. C. (2003) Cosmochemical estimates of mantle composition. In *Treatise on Geochemistry. Vol. 2: The Mantle and Core* (ed. H. D. Holland). Elsevier Pergamon, Oxford, pp. 1–38.
- Pownceby M. I. and O'Neill H. S. C. (1994) Thermodynamic data from redox reactions at high-temperatures. 4. Calibration of the Re-ReO_2 oxygen buffer from Emf and $\text{NiO}+\text{Ni-Pd}$ redox sensor measurements. *Contrib. Mineral. Petrol.* **118**, 130–137.
- Righter K. (2005) Highly Siderophile elements: Constraints on Earth Accretion and Early Differentiation. In *The Earth's Deep Mantle*, vol. 160 (ed. V. D. Hilst et al.). AGU Geophysical Monograph Series, pp. 201–218.
- Righter K. and Drake M. J. (1997) Metal-silicate equilibrium in a homogeneously accreting earth: new results for Re. *Earth Planet. Sci. Lett.* **146**, 541–553.
- Righter K. and Drake M. J. (2003) Partition coefficients at high pressure and temperature. In *Treatise on Geochemistry. The Mantle and Core*, vol. 2 (ed. H. D. Holland et al.). Elsevier Pergamon, Oxford, pp. 425–449.
- Righter K., Drake M. J. and Yaxley G. (1997) Prediction of siderophile element metal-silicate partition coefficients to 20 GPa and 2800 °C: the effects of pressure, temperature, oxygen fugacity, and silicate and metallic melt compositions. *Phys. Earth Planet. Inter.* **100**, 115–134.
- Righter K., Humayun M. and Danielson L. (2008) Partitioning of palladium at high pressures and temperatures during core formation. *Nat. Geosci.* **1**, 321–323.
- Ringwood A. E. (1977) Composition of core and implications for origin of Earth. *Geochem. J.* **11**, 111–135.
- Rubie D. C., Frost D. J., Mann U., Asahara Y., Nimmo F., Tsuno K., Kegler P., Holzheid A. and Palme H. (2011) Heterogeneous accretion, composition and core-mantle differentiation of the Earth. *Earth Planet. Sci. Lett.* **301**, 31–42.
- Rubie D. C., Melosh H. J., Reid J. E., Liebske C. and Righter K. (2003) Mechanisms of metal-silicate equilibration in the terrestrial magma ocean. *Earth Planet. Sci. Lett.* **205**, 239–255.
- Sanchez-Valle C. and Bass J. D. (2010) Elasticity and pressure-induced structural changes in vitreous MgSiO_3 -enstatite to lower mantle pressures. *Earth Planet. Sci. Lett.* **295**, 523–530.
- Sylvester P. J. and Eggins S. M. (1997) Analysis of Re, Au, Pd, Pt and Rh in NIST glass certified reference materials and natural basalt glasses by laser ablation ICP-MS. *Geostand. Newslett.: J. Geostand. Geoanal.* **21**, 215–230.
- Thibault Y. and Walter M. J. (1995) The influence of pressure and temperature on the metal-silicate partition-coefficients of nickel and cobalt in a model-C1 chondrite and implications for metal segregation in a deep magma ocean. *Geochim. Cosmochim. Acta* **59**, 991–1002.
- Wade J. and Wood B. J. (2005) Core formation and the oxidation state of the Earth. *Earth Planet. Sci. Lett.* **236**, 78–95.
- Walker R. J. (2009) Highly siderophile elements in the Earth, Moon and Mars: update and implications for planetary accretion and differentiation. *Chemie der Erde - Geochemistry* **69**, 101–125.
- Walter M. J., Newsom H. E., Ertel W. and Holzheid A. (2000) Siderophile elements in the Earth and Moon: metal/silicate partitioning and implications for core formation. In *Origin of the Earth and Moon* (eds. R. M. Canup and K. Righter). The Univ. of Arizona space science series, pp. 265–289.
- Wood B. J. and Halliday S. L. (2010) The lead isotopic age of the Earth can be explained by core formation alone. *Nature* **465**, 767–770.
- Yokoyama T., Walker D. and Walker R. J. (2009) Low osmium solubility in silicate at high pressures and temperatures. *Earth Planet. Sci. Lett.* **279**, 165–173.
- Zerr A., Diegeler A. and Boehler R. (1998) Solidus of Earth's deep mantle. *Science* **281**, 243–246.

Associate editor: Richard J. Walker